Phase Field Model of Hydraulic Fracturing in Poroelastic Media: Fracture Propagation, Arrest, and Branching Under Fluid Injection and Extraction

AGU PUBLICATIONS

JGR

Journal of Geophysical Research: Solid Earth

RESEARCH ARTICLE
10.1002/2017JB014740

Key Points:
- We extend our validated phase field model of fluid-driven fracturing from elastic media to poroelastic media
- We model flow in the fracture on a lower-dimension manifold with a nonlocal definition of fracture aperture
- We assess our model by simulating fracture propagation and arrest in the quarter five-spot configuration

Correspondence to:
D. Santillán,
david.santillan@upm.es

Citation:
Santillán, D., Juanes, R., & Cueto-Felgueroso, L. (2018). Phase field model of hydraulic fracturing in poroelastic media: Fracture propagation, arrest, and branching under fluid injection and extraction. *Journal of Geophysical Research: Solid Earth*, *123*. https://doi.org/10.1002/2017JB014740

Received 19 JUL 2017
Accepted 26 JAN 2018
Accepted article online 5 FEB 2018

Phase Field Model of Hydraulic Fracturing in Poroelastic Media: Fracture Propagation, Arrest, and Branching Under Fluid Injection and Extraction

David Santillán[1], **Ruben Juanes**[2,3], **and Luis Cueto-Felgueroso**[1,2]

[1]Departamento de Ingeniería Civil: Hidráulica, Energía y Medio Ambiente, Universidad Politécnica de Madrid, Madrid, Spain, [2]Department of Civil and Environmental Engineering, Massachusetts Institute of Technology, Cambridge, MA, USA, [3]Department of Earth, Atmospheric and Planetary Sciences, Massachusetts Institute of Technology, Cambridge, MA, USA

Abstract The simulation of fluid-driven fracture propagation in a porous medium is a major computational challenge, with applications in geosciences and engineering. The two main families of modeling approaches are those models that represent fractures as explicit discontinuities and solve the moving boundary problem and those that represent fractures as thin damaged zones, solving a continuum problem throughout. The latter family includes the so-called phase field models. Continuum approaches to fracture face validation and verification challenges, in particular grid convergence, well posedness, and physical relevance in practical scenarios. Here we propose a new quasi-static phase field formulation. The approach fully couples fluid flow in the fracture with deformation and flow in the porous medium, discretizes flow in the fracture on a lower-dimension manifold, and employs the fluid flux between the fracture and the porous solid as coupling variable. We present a numerical assessment of the model by studying the propagation of a fracture in the quarter five-spot configuration. We study the interplay between injection flow rate and rock properties and elucidate fracture propagation patterns under the leak-off toughness dominated regime as a function of injection rate, initial fracture length, and poromechanical properties. For the considered injection scenario, we show that the final fracture length depends on the injection rate, and three distinct patterns are observed. We also rationalize the system response using dimensional analysis to collapse the model results. Finally, we propose some simplifications that alleviate the computational cost of the simulations without significant loss of accuracy.

1. Introduction

The simulation of hydraulic fracturing processes has recently emerged as an active research topic in petroleum engineering and environmental science. The growing interest stems from its technical complexity and from its engineering applications in various subsurface energy technologies, including oil and gas production from unconventional low-permeability reservoirs (Cueto-Felgueroso & Juanes, 2013; Economides & Nolte, 2000; Patzek et al., 2013), enhanced geothermal energy systems (Legarth et al., 2005), and coalbed methane production (Moore, 2012). Hydraulic fracturing involves the injection of a fluid at high pressure in order to create artificial fractures, which act as high-permeability pathways (Hubbert & Willis, 1972). An important environmental concern is that these pathways may also unintentionally provide enhanced hydraulic connectivity between the reservoir and the surrounding environment, leading to leakage of fracturing fluid or gas out of the reservoir with the potential for groundwater contamination (Osborn et al., 2011; Vidic et al., 2013). Both perspectives of petroleum engineering and environmental stewardship need rigorous mathematical models and numerical simulation tools capable of describing the essential flow and mechanical processes controlling the growth of hydraulic fractures in porous rocks (Cai & Ofterdinger, 2014; Reagan et al., 2015).

Fluid-driven fracture propagation in elastic media can be simulated through analytical and numerical models. Analytical solutions are available for simple injection protocols and fracture geometries. The medium is considered to be homogeneous and elastic with constant far field stress. Detournay (2016) provides a review of the state-of-the-art of analytical solutions for the penny-shape fracture propagation. Full-physics numerical modeling, however, is needed in practice for the study of more complex systems.

Numerical models can follow either a discrete or a continuous approach. The discrete approach considers the intact rock and the fractures separately, and discontinuities are introduced in the solid. The simplest way to propagate fractures is by splitting nodes (Fu et al., 2013) or breaking elements (Wangen, 2011). Two drawbacks of these techniques are the change in the topology of the discretization, and the restriction of the fracture to propagate following mesh lines. These limitations can be partially overcome by remeshing techniques (Bouchard et al., 2003) or using advanced approaches. Some advanced methodologies include the so-called cohesive zone modeling that relates traction to displacement jumps through constitutive laws (Carrier & Granet, 2012), or the enriched displacement field methods that locate discontinuities inside the finite elements, so that the formulation is enhanced with additional discontinuous-displacement modes (Haghighat & Pietruszczak, 2016; Moës et al., 1999). Other approaches are those based on the spring network methods (Hafver et al., 2014), where fractures are propagated by splitting springs.

Continuum approaches represent the intact rock and the fractures as a single continuum. The topology of the discretization is preserved and discontinuities are not introduced. Examples of continuous approaches include peridynamics (Ouchi et al., 2015), damage mechanics (Shojaei et al., 2014), or phase field models. The latter regularizes discontinuities using a scalar auxiliary variable, the phase field, that smears the fracture surface and interpolates between the broken and unbroken regions.

A broad family of phase field models for fracture mechanics emerged within the physics community on the basis of the work of Aranson et al. (2000), who proposed a continuum-field model for mode-I crack propagation in brittle amorphous solids. This idea has been further developed by many other authors, including Eastgate et al. (2002), Henry and Levine (2004), Karma et al. (2001), Karma and Lobkovsky (2004), or Spatschek et al. (2011).

Independently, a second family emerged in the mechanics community inspired in the works of Ambrosio and Tortorelli (1990), who proposed a phase field approximation of the Mumford-Shah potential (Mumford & Shah, 1989) based on Γ-convergence. Inspired in these works, Francfort and Marigo (1998) proposed a variational formulation for brittle fracture based on the minimization of the combined elastic energy in the bulk material and the fracture energy. The numerical implementation of this formulation was developed by Bourdin et al. (2000), who defined an auxiliary variable—the phase field—that distributes the fracture energy over the bulk material. In practical implementations, both families yield fairly similar numerical schemes (Ambati et al., 2015).

An alternative quasi-static formulation of this phase field approximation has been proposed by Miehe, Welschinger, and Hofacker (2010), based on continuum mechanics and thermodynamical principles. This framework was extended to dynamic problems (Hofacker & Miehe, 2012, 2013), coupled to thermomechanic problems at large strains (Miehe, Schänzel, & Ulmer, 2015), and adapted to simulate ductile fracture coupled with thermoplasticity at finite strains (Miehe, Hofacker, et al., 2015). It has been validated using experimental observations and applied to academic engineering problems for simulating the fracture of two full-scale concrete dams (Santillán et al., 2017a) and to characterize the influence of heterogeneous mechanical properties on the trajectories of hydraulic fractures propagating in elastic media (Santillán et al., 2017b).

Phase field models have been applied to model fluid-driven brittle fracturing. One of the first models was developed by Bourdin et al. (2012), who proposed a phase field model to simulate hydraulic fracturing through linear elastic impermeable materials. Mikelić et al. (2015a, 2015b) developed a phase field model for fracture propagation through fluid-saturated poroelastic materials. The poroelastic domain is described with the Biot linear model at infinitesimal strains, and the flow in the fracture with the Reynolds lubrication equation. Following the philosophy of the diffusive crack topology, the latter is described in the same dimension as the solid and both are coupled via a pressure diffraction equation, that is, a single pressure equation for both domains with discontinuous coefficients. Coefficients depend on the phase field variable in a way that the generalized pressure equation becomes Darcy's law in the reservoir domain and the Reynolds equation in the fracture domain. In the transition zone from undamaged to damaged regions a combination of both is adopted, and interface conduction is imposed to account for fluid exchange between both regions. The permeability of the fracture depends on the aperture, which is computed with the normal displacement of the points adjacent to the fracture. The model has been improved with remeshing techniques (Lee, Wheeler, et al., & Wick, 2016), level-set approaches to compute the fracture aperture (Lee, Mikelić, et al., 2016), and has been extended to simulate proppant transport in the fractures (Lee et al., 2017).

Miehe, Mauthe, and Teichtmeister (2015) developed a full variational framework for phase field fracture in poroelastic materials at finite strains. This work has been extended to simulate fluid-driven fracture propagation (Miehe & Mauthe, 2016) and adapted to infinitesimal strains (Mauthe & Miehe, 2017). Fractures are modeled by adding an additional term into the Darcy permeability tensor, which accounts for the Reynolds lubrication theory and fluid interchange between the fracture and the porous solid. The additional permeability is multiplied by a term that grows with the damage. Fractures are then described in the same dimension as the solid. The fracture opening, necessary for determining the fracture permeability, is computed in terms of the normal deformation to the fracture and multiplied by a length scale associated with the size of the numerical discretization.

Wilson and Landis (2016) developed a phase field model at large strains through fundamental balance laws and Coleman–Noll-type procedures. The porous solid is modeled following the Biot theory, and flow inside the fractures with the Stokes equation. Both flow regimes are simultaneously described by using indicator functions of the phase field. Heider and Markert (2017) proposed a phase field model embedded in the theory of porous media to simulate fluid-driven fracturing in poroelastic media based on the Allen-Cahn diffusion model for the evolution of the phase field. The evolution of the fracture is accounted for by updating the porosity of the solid, which is expressed as function of the phase field variable and the material deformation gradient of the solid. Moreover, flow in the porous solid is described through Darcy's law and inside the fracture through Stokes flow. The formulation takes into account the transition between flow regimes by using indicator functions which depend on the porosity.

The reported approaches describe fractures as diffuse entities with the same dimension as the solid. Flow in the porous medium is modeled through Darcy's law and in the fracture through lubrication theory or Stokes flow, and both in the same dimension. During the fracture propagation, the fluid flow changes from one regime to another and is modeled through indicator functions which depend on the damage variable. Since the damage variable smears the fracture interface, the transition between both flow regimes is also smoothed. Moreover, this transition is conditioned by the shape of the indicator functions, and the results of the simulations may depend on the choice for these functions.

Here we propose another framework for the simulation of fluid-driven fractures in poroelastic solids using the phase field approach. We treat fractures as diffuse entities with the same dimension as the solid for the mechanical problem, *but we describe the fracture flow in a lower dimensional manifold through lubrication theory*. The fracture aperture, and the deformation and pressure of the porous solid are solved in a fully coupled fashion employing two separate meshes for each domain (fracture and poroelastic solid) which are coincident in space. We adopt the distributed fluid flux between both domains as the coupling variable, inspired in the strategy of some discrete approaches (Réthoré et al., 2007). This framework has been validated for elastic solids by comparing with analytical solutions (Santillán, Juanes, & Cueto-Felgueroso, 2017), and here we extend the formulation to poroelastic solids. We apply our model to study the propagation of a single existing fracture in the quarter five-spot configuration. We study the different fracture propagation patterns, and we elucidate the effect of several hydromechanical characteristics, such as injection flow rate or medium permeability, on the final fracture topology. Finally, we perform a dimensional analysis to isolate the controlling dimensionless groups and demonstrate the physical consistency of the model.

The paper is organized as follows: in section 2 we describe the mathematical formulation of the model. In section 3 we present several analytical models employed to assess the numerical framework. In section 4 we introduce the quarter five-spot problem that we study and present and analyze the modeling results. Finally, we present conclusions in section 5.

2. Phase Field Modeling of Hydraulic Fracture

The mathematical modeling approach used in this study is presented in two steps for clarity. We start with the basic equations of linear poroelasticity, which will characterize the coupled flow and mechanics of intact rock, and the Reynolds lubrication equation, which will describe the flow in the fracture. After introducing the poroelastic equations, we turn to explaining the regularized damage model, built using the phase field modeling framework and the variational approach to fracture.

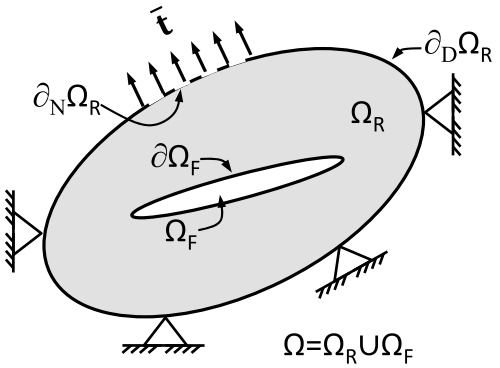

Figure 1. Schematic of the problem domains and boundary conditions, where we define an intact rock domain (subscript *R*), and a fracture domain (subscript *F*).

2.1. Field Equations of Poroelasticity and Fluid Flow in the Fracture

For a fluid-saturated medium, and assuming Darcy flow, the Biot equations of poroelasticity summarize the coupling between solid and fluid mass conservation, and mechanical equilibrium (Biot, 1941, 1972):

$$\alpha\frac{\partial\varepsilon_v}{\partial t}+\frac{1}{M}\frac{\partial p}{\partial t}=\nabla\cdot\left(\frac{\kappa}{\mu_f}\left(\nabla p-\rho_f\mathbf{a_g}\right)\right)+q_{fm}, \tag{1}$$

$$\nabla\cdot\boldsymbol{\sigma}=-\mathbf{f}, \tag{2}$$

where α is the Biot coefficient, ε_v is the volumetric strain, $\varepsilon_v=\mathrm{tr}\,(\boldsymbol{\varepsilon})$, $\boldsymbol{\varepsilon}$ is the strain tensor, t is time, M is the Biot modulus, p is the pressure field, κ is the intrinsic permeability of the porous medium, μ_f is the fluid dynamic viscosity, ρ_f is the fluid density, $\mathbf{a_g}$ is the gravity acceleration, q_{fm} is the source or sink term between the fracture and the poroelastic medium, σ is the total stress tensor, and $\mathbf{f}$ is the body force per unit volume.

We assume that the porous medium is a linear elastic material, undergoing small deformations. Thus, the effective stress tensor, $\boldsymbol{\sigma}'=\boldsymbol{\sigma}+\alpha p\mathbf{I}$, is a linear function of strains as

$$\boldsymbol{\sigma}'=\lambda\mathrm{tr}(\boldsymbol{\varepsilon})\mathbf{I}+2\mu\boldsymbol{\varepsilon}, \tag{3}$$

where λ and μ are the Lamé constants, $\boldsymbol{\varepsilon}$ is the infinitesimal strain tensor, $\boldsymbol{\varepsilon}=\frac{1}{2}\left(\nabla\mathbf{u}+\nabla\mathbf{u}^T\right)$, and $\mathbf{u}$ is the displacement field. The above equations govern the coupled flow and rock mechanical deformation of saturated flow through a linear elastic porous material.

The fluid flow in the fracture is described by the lubrication theory and is considered to take place *on a lower dimensional manifold*. The fluid motion is given by the Reynolds lubrication equation as

$$\frac{\partial w}{\partial t}+c_f w\frac{\partial p_F}{\partial t}=\nabla_s\cdot\left(\frac{w^2}{12\mu_f}\left(\nabla_s p_F-\rho_f a_g\nabla_s z\right)\right)+q_{mf},\quad \text{in } \Omega_F, \tag{4}$$

where w is the fracture aperture, c_f is the fluid compressibility, p_F is the fluid pressure inside the fracture, z is the elevation, s is the longitudinal coordinate along the fracture, and q_{mf} is the source or sink flow rate between the poroelastic medium and the fracture.

2.2. Variational Approach to Rock Damage and Brittle Fracture

Let us consider a domain $\Omega\subset\mathfrak{R}^\delta$ with spatial dimension $\delta\in[2,3]$, composed by a poroelasic reservoir domain Ω_R and a pressurized fracture domain Ω_F, that is, $\Omega=\Omega_R\cup\Omega_F$ (see Figure 1). The boundary of Ω_i is denoted by $\partial\Omega_i$, where $i=R,F$. Homogeneous Dirichlet conditions for the displacements are imposed on $\partial_D\Omega_i$, and Neumann conditions on $\partial_N\Omega_i$, with $\partial_D\Omega_i\cup\partial_N\Omega_i=\partial\Omega_i$ and $\partial_D\Omega_i\cap\partial_N\Omega_i=\emptyset$. The outward unit normal to $\partial\Omega$ is $\mathbf{n}$.

We adopt the Griffith interpretation to model quasi-static brittle fracture propagation, which states that the elastic energy release during the fracture process is balanced by newly created surface energy as the fracture propagates (Griffith, 1921). Based on this idea, Francfort and Marigo (1998) developed a variational formulation based on the minimization of the total potential energy, that is, the system adopts the configuration whose potential energy is minimized.

The potential energy Ψ has four components: the energy dissipated in the fracturing process Ψ^d, the energy stored in the bulk of the solid Ψ^e, the energy stored in the fluid Ψ^f, and the external sources of energy Ψ^s,

$$\Psi=\Psi^d+\Psi^e+\Psi^f-\Psi^s. \tag{5}$$

The energy dissipated in the fracturing process, Ψ^d, is the work required to create a unit fracture area,

$$\Psi^d=\int_{\partial\Omega_F}g_c\,\mathrm{d}\partial, \tag{6}$$

where g_c is the Griffith critical energy release rate for mode I failure. The integral in equation (6) is extended to the boundary of the fracture domain, which a priori is unknown. The regularization of the fracture surface allows us to extend equation (6) to the whole domain,

$$\Psi^d=\int_\Omega g_c\gamma_\ell\,\mathrm{d}\Omega, \tag{7}$$

where γ_ℓ is the fracture density that serves as a smoothed indicator function, and it is given by (Miehe, Welschinger, & Hofacker, 2010):

$$\gamma_\ell = \frac{1}{2\ell} d^2 + \frac{\ell}{2} |\nabla d|^2 , \tag{8}$$

where d is the phase field variable, and ℓ is a length scale parameter. d is the key new variable that is introduced as damage variable and interpolates between the broken state, $d = 1$, and the unbroken one, $d = 0$.

The energy stored in the undamaged bulk of the solid, Ψ_0^e, reads

$$\Psi_0^e = \int_\Omega \psi_0^e(\boldsymbol{\varepsilon})\, \mathrm{d}\Omega, \tag{9}$$

where ψ_0^e is the undamaged elastic energy density, given by

$$\psi_0^e(\boldsymbol{\varepsilon}) = \frac{\lambda}{2}\mathrm{tr}(\boldsymbol{\varepsilon})^2 + \mu \mathrm{tr}(\boldsymbol{\varepsilon}^2). \tag{10}$$

The loss of stiffness of the solid due to the fracturing process implies that it cannot store the same amount of energy as it degrades. The degradation can be modeled mathematically in two ways (Miehe, Welschinger, & Hofacker, 2010): the *isotropic* and the *anisotropic* formulations. The isotropic formulation considers the degradation of the whole elastic energy regardless of the sign of stress. The anisotropic formulation, in contrast, allows for degradation in tension only. We adopt the latter since it provides more realistic results. The damaged elastic energy, Ψ^e, is then given by

$$\Psi^e = \int_\Omega \left[g(d)\psi_0^{e+}(\boldsymbol{\varepsilon}) + \psi_0^{e-}(\boldsymbol{\varepsilon}) \right] \mathrm{d}\Omega = \int_\Omega \psi^e(\boldsymbol{\varepsilon}, d)\, \mathrm{d}\Omega, \tag{11}$$

where ψ_0^{e+} is the part of the undamaged elastic energy generated by tension, ψ_0^{e-} is the part generated by compression, and $g(d)$ is the degradation function. A common expression for $g(d)$ is (Vignollet et al., 2014)

$$g(d) = (1 - d)^2. \tag{12}$$

Each part of the undamaged energy is defined as follows:

$$\psi_0^{e\pm}(\boldsymbol{\varepsilon}) = \frac{\lambda}{2}\left(\left\langle \sum_{a=1}^{\delta} \varepsilon_a \right\rangle_\pm \right)^2 + \mu \sum_{a=1}^{\delta} \left(\langle \varepsilon_a \rangle_\pm \right)^2 , \tag{13}$$

where ε_a is the ath principal strain, and $\langle x \rangle_\pm = (x \pm |x|)/2$. The decomposition fulfills

$$\psi_0^e(\boldsymbol{\varepsilon}) = \psi_0^{e+}(\boldsymbol{\varepsilon}) + \psi_0^{e-}(\boldsymbol{\varepsilon}). \tag{14}$$

The resulting effective stress-strain constitutive relation is defined as follows:

$$\boldsymbol{\sigma}'(\mathbf{u}, d) := g(d)\frac{\partial \psi_0^{e+}}{\partial \boldsymbol{\varepsilon}} + \frac{\partial \psi_0^{e-}}{\partial \boldsymbol{\varepsilon}}, \tag{15}$$

or alternatively

$$\boldsymbol{\sigma}'^{+}(\mathbf{u}, d) = g(d) \sum_{a=1}^{\delta} \left[\lambda \left\langle \sum_{i=1}^{\delta} \varepsilon_i \right\rangle_+ + 2\mu \langle \varepsilon_a \rangle_+ \right] \mathbf{n}_a \otimes \mathbf{n}_a, \tag{16}$$

and

$$\boldsymbol{\sigma}'^{-}_0(\mathbf{u}) = \boldsymbol{\sigma}'^{-}(\mathbf{u}) = \sum_{a=1}^{\delta} \left[\lambda \left\langle \sum_{i=1}^{\delta} \varepsilon_i \right\rangle_- + 2\mu \langle \varepsilon_a \rangle_- \right] \mathbf{n}_a \otimes \mathbf{n}_a, \tag{17}$$

where $\mathbf{n}_a$ is the principal strain direction associated to the principal strain ε_a. The eigenvalue bases $\mathbf{n}_a \otimes \mathbf{n}_a$ are computed in terms of the principal strains ε_i, where $i = a, b$, and the strain tensor, $\boldsymbol{\varepsilon}$, as follows (Miehe, 1998):

$$\mathbf{n}_a \otimes \mathbf{n}_a = \frac{1}{\prod_{b\neq a}^{\delta} (\varepsilon_a - \varepsilon_b)} \prod_{b\neq a}^{\delta} (\boldsymbol{\varepsilon} - \varepsilon_b \mathbf{1}) . \tag{18}$$

The potential energy stored in the fluid, Ψ^f, reads

$$\Psi^f = \int_{\Omega_R} \psi^f(p, \nabla \cdot \mathbf{u})\, \mathrm{d}\Omega, \tag{19}$$

where ψ^f is the potential energy density of the fluid, defined as

$$\psi_0^f(p, \nabla \cdot \mathbf{u}) = -p\alpha \nabla \cdot \mathbf{u}. \tag{20}$$

The integral in equation (19) is extended over the reservoir, whose domain changes with time. We avoid this difficulty by using the degradation function, $g(d)$, and extending the integral over the whole domain and localizing its effect at the interface through the degradation function as follows:

$$\Psi^f = \int_{\Omega_R} \psi^f(p, \nabla \cdot \mathbf{u})\, \mathrm{d}\Omega = \int_{\Omega} g(d)\psi^f(p, \nabla \cdot \mathbf{u})\, \mathrm{d}\Omega = -\int_{\Omega} g(d)p\alpha \nabla \cdot \mathbf{u}\, \mathrm{d}\Omega. \tag{21}$$

The external energy functional, Ψ^s, is given by

$$\Psi^s = \int_{\Omega} \mathbf{f} \cdot \mathbf{u}\, \mathrm{d}\Omega + \int_{\partial_N \Omega} \mathbf{t} \cdot \mathbf{u}\, \mathrm{d}\partial, \tag{22}$$

where $\mathbf{t}$ is the vector of applied forces. The second term includes the force introduced by the pressure inside the fracture, which is applied on a surface which, a priori, is unknown:

$$\int_{\partial_N \Omega_F} \mathbf{t} \cdot \mathbf{u}\, \mathrm{d}\partial = -\int_{\partial_N \Omega_F} p_F \mathbf{n} \cdot \mathbf{u}\, \mathrm{d}\partial. \tag{23}$$

The pressure continuity at $\partial\Omega_F$ implies that we can use the pressure field p, which fulfills $p = p_F$ in Ω_F and $p = p_R$ in Ω_R. Equation (23) can be interpreted as a flux of energy through the surface of the fracture. Using the divergence theorem, we rewrite the equation as

$$\int_{\partial_N \Omega_F} p\mathbf{n} \cdot \mathbf{u}\, \mathrm{d}\partial = \int_{\Omega_R} \nabla \cdot (p\mathbf{u})\, \mathrm{d}\Omega - \int_{\partial_N \Omega_R} p\mathbf{n} \cdot \mathbf{u}\, \mathrm{d}\partial. \tag{24}$$

By using the degradation function, $g(d)$, the previous integral is redefined over the whole domain (Mikelić et al., 2015b):

$$\int_{\Omega_R} \nabla \cdot (p\mathbf{u})\, \mathrm{d}\Omega = \int_{\Omega} g(d) \nabla \cdot (p\mathbf{u})\, \mathrm{d}\Omega. \tag{25}$$

Therefore, the external energy functional Ψ^s reads

$$\Psi^s = \int_{\Omega} \mathbf{f} \cdot \mathbf{u}\, \mathrm{d}\Omega - \int_{\Omega} g(d) \nabla \cdot (p\mathbf{u})\, \mathrm{d}\Omega + \int_{\partial_N \Omega_R} p\mathbf{n} \cdot \mathbf{u}\, \mathrm{d}\partial + \int_{\partial_N \Omega_R} \mathbf{t} \cdot \mathbf{u}\, \mathrm{d}\partial. \tag{26}$$

We derive the strong form of the problem via minimization of the total potential energy, Ψ, with respect to $\mathbf{u}$ and d. The Fréchet derivative of Ψ with respect to $\mathbf{u}$ provides the equilibrium equations:

$$\frac{\partial \Psi}{\partial \mathbf{u}} - \nabla \cdot \left(\frac{\partial \Psi}{\partial \nabla \mathbf{u}} \right) = \mathbf{0}, \quad \text{in } \Omega, \tag{27}$$

$$\frac{\partial \Psi}{\partial \nabla \mathbf{u}} \cdot \mathbf{n} = \mathbf{t}, \quad \text{in } \partial_N \Omega. \tag{28}$$

The equilibrium equations are as follows:

$$-\nabla \cdot \left\{ g(d)\boldsymbol{\sigma'}_0^+ + \boldsymbol{\sigma'}_0^- \right\} + \nabla \{\alpha g(d)p\} - \nabla \{g(d)p\} + g(d)\nabla p - \mathbf{f} = \mathbf{0}, \quad \text{in } \Omega, \tag{29}$$

$$g(d)\boldsymbol{\sigma'}_0^+ \mathbf{n} + \boldsymbol{\sigma'}_0^- \mathbf{n} + (1-\alpha)g(d)p\mathbf{n} = \mathbf{t}, \quad \text{in } \partial_N \Omega. \tag{30}$$

Equation (29) can be rewritten as

$$-\nabla \cdot \left\{ g(d)\boldsymbol{\sigma'}_0^+ + \boldsymbol{\sigma'}_0^- \right\} + \nabla \{\alpha g(d)p\} - p\nabla g(d) - \mathbf{f} = \mathbf{0}, \tag{31}$$

or alternatively

$$\nabla \cdot \left\{ \boldsymbol{\sigma'} - \alpha g(d)p\mathbf{1} \right\} + p\nabla g(d) + \mathbf{f} = \mathbf{0}, \tag{32}$$

where the first term is the divergence of the total stresses with $\boldsymbol{\sigma'}$ given by equation (15), the second term is the pressure force introduced by the fluid inside the fracture, and the last term is the external body force.

The pressure force from the fluid-filled fracture is handled as a body force by using the gradient of the degradation function. The main advantage of this approach is that there is no need to know the geometry of the fracture.

The Fréchet derivative of Ψ with respect to d,

$$\frac{\partial \Psi}{\partial d} - \nabla \cdot \left(\frac{\partial \Psi}{\partial \nabla d} \right) = 0, \quad \text{in } \Omega, \tag{33}$$

$$\frac{\partial \Psi}{\partial \nabla d} \cdot \mathbf{n} = 0, \quad \text{in } \partial_N \Omega, \tag{34}$$

provides the Euler equations of the phase field problem:

$$\frac{g_c}{\ell} \left(d - \ell^2 \nabla^2 d \right) = 2(1-d) \left(\psi_0^{e+}(\boldsymbol{\varepsilon}) - \alpha p \nabla \cdot \mathbf{u} + \nabla \cdot (p\mathbf{u}) \right), \quad \text{in } \Omega, \tag{35}$$

$$\nabla d \cdot \mathbf{n} = 0, \quad \text{in } \partial_N \Omega. \tag{36}$$

The irreversibility of the fracture process is accounted for by the local history field of maximum positive store energy, H^+, defined as (Miehe, Hofacker, & Welschinger, 2010)

$$H^+(\mathbf{u}, p, t) = \max_{s \in [0,t]} \left(\psi_0^{e+}(\boldsymbol{\varepsilon}) - (\alpha - 1) p \nabla \cdot \mathbf{u} + \mathbf{u} \cdot \nabla p \right). \tag{37}$$

The Euler equation of the phase field is then written as follows:

$$\frac{g_c}{\ell} \left(d - \ell^2 \nabla^2 d \right) = 2(1-d) H^+. \tag{38}$$

2.3. Summary of Governing Equations

The phase field mathematical model comprises four partial differential equations, modeling mass conservation in the poroelastic medium, fluid flow inside the fracture, mechanical equilibrium, and phase field. The mass conservation equation in the poroelastic medium is given by the Biot equation of poroelasticity (Biot, 1941, 1972)

$$\alpha \frac{\partial \varepsilon_v}{\partial t} + \frac{1}{M} \frac{\partial p}{\partial t} = \nabla \cdot \left(\frac{\kappa}{\mu_f} \left(\nabla p - \rho_f \mathbf{a_g} \right) \right) + q_{fm}. \tag{39}$$

The fluid flow inside the fracture is described through the Reynolds lubrication equation

$$\frac{\partial w}{\partial t} + C_f w \frac{\partial p}{\partial t} = \nabla_s \cdot \left(\frac{w^2}{12 \mu_f} \left(\nabla_s p - \rho_f a_g \nabla_s z \right) \right) + q_{mf}, \quad \text{in } \Omega_F, \tag{40}$$

where $q_{mf} = -q_{fm}$, except at the injection or extraction points. The third equation is the mechanical equilibrium,

$$\nabla \cdot \left\{ \boldsymbol{\sigma}' - \alpha g(d) p \mathbf{1} \right\} + p \nabla g(d) + \mathbf{f} = \mathbf{0}, \tag{41}$$

where $\boldsymbol{\sigma}'$ is given by equation (15). The last equation is the phase field equation,

$$\frac{g_c}{\ell} \left(d - \ell^2 \nabla^2 d \right) = 2(1-d) H^+, \tag{42}$$

where

$$H^+(\mathbf{u}, p, t) = \max_{s \in [0,t]} \left(\psi_0^{e+}(\boldsymbol{\varepsilon}) - (\alpha - 1) p \nabla \cdot \mathbf{u} + \mathbf{u} \cdot \nabla p \right). \tag{43}$$

2.4. Numerical Implementation

The governing equations (39)–(43) constitute a nonlinear system of partial differential equations. The equilibrium equation (41) includes a nonlinear stress-strain relation due to the spectral decomposition of the strain tensor and the presence of the phase field variable. The nonlinearity is handled with a *hybrid* formulation for the stress-strain relationship (Ambati et al., 2015), combined with a staggered scheme for updating the fields involved (Miehe, Hofacker, & Welschinger, 2010).

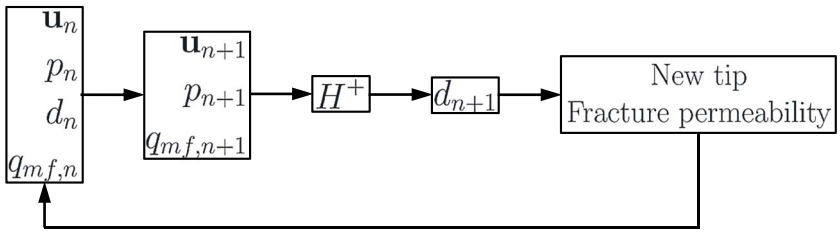

Figure 2. Flow chart of the staggered scheme.

The idea behind the hybrid formulation for the spectral decomposition of the strain tensor is to retain a linear equilibrium equation within a staggered algorithm. The formulation requires the stress-strain relationship

$$\boldsymbol{\sigma}'(\mathbf{u}, d) := g(d)\frac{\partial \psi_0^e}{\partial \boldsymbol{\varepsilon}} \tag{44}$$

combined with the phase field equation (42), where the evolution of d is driven by the tensile energy ψ_0^{e+}. In the case that the sides of the fracture touch each other, the interpenetration is avoided by the constrain:

$$\forall\, \mathbf{x} \quad : \quad \Psi_0^{e+} < \Psi_0^{e-} \quad \Rightarrow \quad d := 0, \tag{45}$$

imposed in the phase field equation (42). The hybrid formulation provides physical results for fracture evolution that are similar to those of the anisotropic formulation (Ambati et al., 2015).

We adopt the staggered scheme proposed by Miehe, Hofacker, and Welschinger (2010) for computing all the fields involved in our problem, which is a simple and robust alternative to the monolithic scheme. The scheme in the time interval $[t_n, t_{n+1}]$ consists of four steps, Figure 2. We assume that all fields are known at time t_n.

1. First, $\mathbf{u}$, p, Q_{mf}, and w are updated using a fully coupled scheme with frozen d, and fracture permeability, equations (39)–(41).
2. Then, H^+ is updated with the values of $\mathbf{u}_{n+1}$ and p_{n+1}, equation (43).
3. Afterward, d_{n+1} is computed with the updated value of H^+, equation (42).
4. Finally, the tip of the fracture is updated with the value of d_{n+1}, as well as the fracture permeability.

This strategy combined with the hybrid formulation has been applied to mechanical problems, with results of comparable quality to the most complex schemes (Ambati et al., 2015). However, the scheme requires small loading increments to properly capture the nonlinearity and strong coupling of the problem.

2.4.1. Numerical Implementation of the Hydromechanical Problem

The first step of the computational scheme involves the solution of the coupled governing equations of flow and rock mechanics. We approximate the equations using a finite volume scheme on a Cartesian regular quadrilateral mesh for the spatial discretization (Demirdžić & Martinović, 1993; Nordbotten, 2014). Pressure, p, displacement, $\mathbf{u}$, and fracture-matrix flux, q_{fm}, are solved in a monolithically coupled fashion, using a Backward Euler scheme for the time integration. The starting point for the finite volume formulation of the flow problem is the integral form of the conservation law (39) over an arbitrary control volume Ω,

$$\int_\Omega \alpha \frac{\partial \varepsilon_v}{\partial t} \mathrm{d}\Omega + \int_\Omega \frac{1}{M}\frac{\partial p}{\partial t}\mathrm{d}\Omega - \int_\Omega \nabla \cdot \left(\frac{\kappa}{\mu_f}\left(\nabla p - \rho_f \mathbf{a_g}\right)\right)\mathrm{d}\Omega - \int_\Omega q_{fm}\mathrm{d}\Omega = 0. \tag{46}$$

Using the divergence theorem, equation (46) is rewritten as

$$\int_\Omega \alpha \frac{\partial \varepsilon_v}{\partial t} \mathrm{d}\Omega + \int_\Omega \frac{1}{M}\frac{\partial p}{\partial t}\mathrm{d}\Omega - \int_{\partial\Omega} \frac{\kappa}{\mu_f}\left(\nabla p - \rho_f \mathbf{a_g}\right)\mathrm{d}\partial\Omega - \int_\Omega q_{fm}\mathrm{d}\Omega = 0, \tag{47}$$

where the volume Ω is bounded by the surface $\partial\Omega$. The discrete equation for the flow in the poroelastic solid is, for a given control volume (i, j) in a regular Cartesian grid and ignoring gravity effects,

$$\begin{aligned} \alpha \frac{\varepsilon_{v,i,j}^{n+1} - \varepsilon_{v,i,j}^{n}}{\delta t}\delta x \delta y + \frac{1}{M}\frac{p_{i,j}^{n+1} - p_{i,j}^{n}}{\delta t}\delta x \delta y + \left[-\lambda_m \frac{\partial p}{\partial x}\right]_{i+1/2,j} + \\ - \left[-\lambda_m \frac{\partial p}{\partial x}\right]_{i-1/2,j} + \left[-\lambda_m \frac{\partial p}{\partial y}\right]_{i,j+1/2} - \left[-\lambda_m \frac{\partial p}{\partial y}\right]_{i,j-1/2} - Q_{fm,i,j}^{n+1} = 0, \end{aligned} \tag{48}$$

where $\lambda_m = \kappa/\mu_f$ is the mobility. The volumetric strains are integrated quantities that we approximate using the divergence theorem. The fully discrete equation is given by

$$\begin{aligned}\alpha\frac{\frac{1}{2}\left(u_{i+1,j}^{n+1}-u_{i-1,j}^{n+1}\right)-\frac{1}{2}\left(u_{i+1,j}^{n}-u_{i-1,j}^{n}\right)}{\delta t}\delta y+\alpha\frac{\frac{1}{2}\left(v_{i,j+1}^{n+1}-v_{i,j-1}^{n+1}\right)-\frac{1}{2}\left(v_{i,j+1}^{n}-v_{i,j-1}^{n}\right)}{\delta t}\delta x+\\ +\frac{1}{M}\frac{p_{i,j}^{n+1}-p_{i,j}^{n}}{\delta t}\delta x\delta y-\lambda_{m,i+1/2,j}\left(\frac{p_{i+1,j}^{n+1}-p_{i,j}^{n+1}}{\delta x}\right)\delta y+\lambda_{m,i-1/2,j}\left(\frac{p_{i,j}^{n+1}-p_{i-1,j}^{n+1}}{\delta x}\right)\delta y+\\ -\lambda_{m,i,j+1/2}\left(\frac{p_{i,j+1}^{n+1}-p_{i,j}^{n+1}}{\delta y}\right)\delta x+\lambda_{m,i,j-1/2}\left(\frac{p_{i,j}^{n+1}-p_{i,j-1}^{n+1}}{\delta y}\right)\delta x-Q_{fm,i,j}^{n+1}=0.\end{aligned} \tag{49}$$

In the above expression, we deliberately allow for a heterogeneous spatial distribution of the mobility. Rearranging the above expression, we arrive at

$$\begin{aligned}&\left(\frac{\delta x\delta y}{M\delta t}+\lambda_{m,i-1/2,j}\frac{\delta y}{\delta x}+\lambda_{m,i+1/2,j}\frac{\delta y}{\delta x}+\lambda_{m,i,j-1/2}\frac{\delta x}{\delta y}+\lambda_{m,i,j+1/2}\frac{\delta x}{\delta y}\right)p_{i,j}^{n+1}+\\ &-\lambda_{m,i+1/2,j}\frac{\delta y}{\delta x}p_{i+1,j}^{n+1}-\lambda_{m,i-1/2,j}\frac{\delta y}{\delta x}p_{i-1,j}^{n+1}-\lambda_{m,i,j+1/2}\frac{\delta x}{\delta y}p_{i,j+1}^{n+1}-\lambda_{m,i,j-1/2}\frac{\delta x}{\delta y}p_{i,j-1}^{n+1}+\\ &+\frac{\alpha\delta y}{2\delta t}\left(u_{i+1,j}^{n+1}-u_{i-1,j}^{n+1}\right)+\frac{\alpha\delta x}{2\delta t}\left(v_{i,j+1}^{n+1}-v_{i,j-1}^{n+1}\right)-Q_{fm,i,j}^{n+1}\\ &=\frac{\delta x\delta y}{M\delta t}p_{i,j}^{n}+\frac{\alpha\delta y}{2\delta t}\left(u_{i+1,j}^{n}-u_{i-1,j}^{n}\right)+\frac{\alpha\delta x}{2\delta t}\left(v_{i,j+1}^{n}-v_{i,j-1}^{n}\right).\end{aligned} \tag{50}$$

The interfacial mobilities are approximated using the harmonic mean:

$$\lambda_{m,i\pm1/2,j}=\frac{2}{\frac{1}{\lambda_{m,i\pm1,j}}+\frac{1}{\lambda_{m,i,j}}},\quad \lambda_{m,i,j\pm1/2}=\frac{2}{\frac{1}{\lambda_{m,i,j\pm1}}+\frac{1}{\lambda_{m,i,j}}}. \tag{51}$$

The flow equation inside the fracture, equation (40), has a lower dimensionality in space. It is solved on a regular compatible one-dimensional (1-D) mesh embedded in the two-dimensional (2-D) domain whose centers of cells or volumes are coincident in space. Ignoring gravity effects, the integral form of the equation is given by

$$\int_\Omega\frac{\partial w}{\partial t}\mathrm{d}\Omega+\int_\Omega C_f w\frac{\partial p}{\partial t}\mathrm{d}\Omega-\int_\Omega\nabla_s\cdot\left(\frac{w^2}{12\mu_f}\nabla_s p\right)\mathrm{d}\Omega-\int_\Omega q_{mf}\mathrm{d}\Omega=0. \tag{52}$$

The divergence theorem yields

$$\int_\Omega\frac{\partial w}{\partial t}\mathrm{d}\Omega+\int_\Omega C_f w\frac{\partial p}{\partial t}\mathrm{d}\Omega-\int_{\partial\Omega}\frac{w^2}{12\mu_f}\nabla_s p\mathrm{d}\partial\Omega-\int_\Omega q_{mf}\mathrm{d}\Omega=0. \tag{53}$$

For a given control cell k whose Cartesian coordinates in the 2-D computational grid are (i,j), we denote its neighbor at the right side as $k+1$ and at the left side as $k-1$ in the 1-D computational grid. The Cartesian coordinates of the neighbors in the 2-D mesh are $(i,j)+1$ and $(i,j)-1$, respectively. The discrete version of the mass conservation equation in the fracture, equation (53), reads

$$\frac{w_{i,j}^{n+1}-w_{i,j}^{n}}{\delta t}\delta s+C_f w_{i,j}^{n}\frac{p_{i,j}^{n+1}-p_{i,j}^{n}}{\delta t}\delta s+\left[-\lambda_f\frac{\partial p}{\partial s}\right]_{k+1/2}-\left[-\lambda_f\frac{\partial p}{\partial s}\right]_{k-1/2}-Q_{mf,i,j}^{n+1}=0, \tag{54}$$

where $\lambda_f = w^2/(12\mu_f)$ is the mobility, and Q_{mf} is the integral form of the matrix-fracture flux q_{mf}. The fully discrete equation is given by

$$\frac{w_{i,j}^{n+1}-w_{i,j}^{n}}{\delta t}\delta s+C_f w_{i,j}^{n}\frac{p_{i,j}^{n+1}-p_{i,j}^{n}}{\delta t}\delta s-\lambda_{f,k+1/2}\frac{p_{(i,j)+1}^{n+1}-p_{i,j}^{n+1}}{\delta_s}+\lambda_{f,k-1/2}\frac{p_{i,j}^{n+1}-p_{(i,j)-1}^{n+1}}{\delta_s}-Q_{mf,i,j}^{n+1}=0. \tag{55}$$

Rearranging the above expression and recalling that $Q_{mf}=-Q_{fm}$, we arrive at

$$\begin{aligned}&\frac{\delta_s}{\delta_t}w_{i,j}^{n+1}+\left(C_f w_{i,j}^{n}\frac{\delta s}{\delta t}+\lambda_{f,k+1/2}\frac{1}{\delta s}+\lambda_{f,k-1/2}\frac{1}{\delta s}\right)p_{i,j}^{n+1}-\frac{\lambda_{f,k+1/2}}{\delta s}p_{(i,j)+1}^{n+1}\\ &-\frac{\lambda_{f,k-1/2}}{\delta s}p_{(i,j)-1}^{n+1}+Q_{fm,i,j}^{n+1}=\frac{\delta_s}{\delta_t}w_{i,j}^{n}+C_f w_{i,j}^{n}\frac{\delta s}{\delta t}p_{i,j}^{n}.\end{aligned} \tag{56}$$

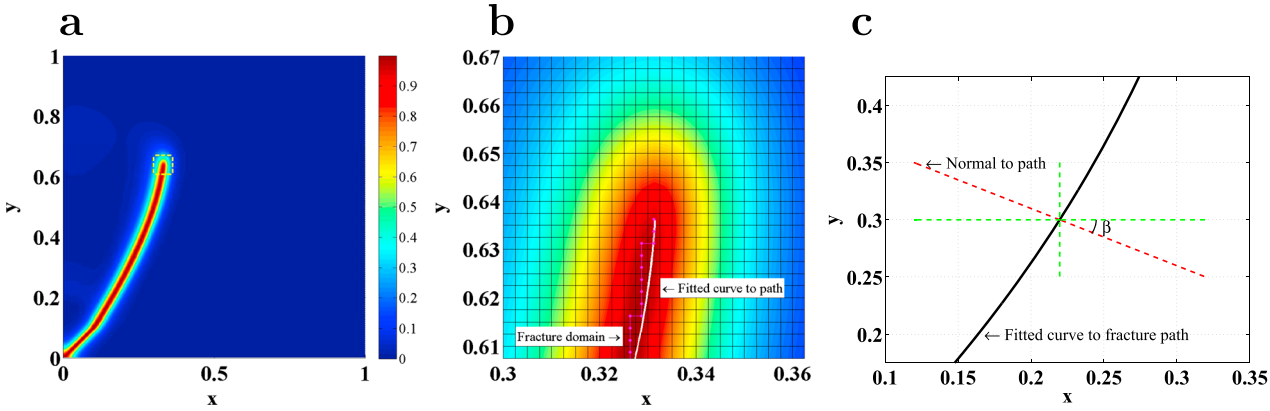

Figure 3. Strategy to propagate the fracture. (a) Here we draw a surface plot of d at time t_n. The fracture propagates following a curve trajectory. (b) We zoom the tip of the fracture. The computational mesh and the integration points are depicted in black. The fracture domain at time t_{n-1} is represented by the solid magenta line, and the fitted curve to the fracture path by the white solid line. (c) We compute the normal to the fracture path through the fitted curved to the trajectory. The normal is defined with the angle β.

The interfacial mobilities are approximated using the harmonic mean as follows:

$$\lambda_{f,k\pm1/2} = \frac{2}{\frac{1}{\lambda_{f,(i,j)\pm1}} + \frac{1}{\lambda_{f,(i,j)}}}. \tag{57}$$

The aperture at point $\mathbf{x}$, $w(\mathbf{x}, \mathbf{u}, d)$, is given by the line integral (Mikelić et al., 2015b)

$$w(\mathbf{x}, \mathbf{u}, d) = \int_a^b \mathbf{u}(r(t)) \cdot \nabla d(r(t)) \left\| r'(t) \right\| \mathrm{d}t, \tag{58}$$

where $r(t)$ is the normal line to the fracture that passes through $\mathbf{x}$. Integral (58) is defined on interval $[a, b]$, whose limits are points sufficiently far away from the ends of the fracture that $\nabla d(r(a))$ and $\nabla d(r(b))$ are negligible.

We evaluate numerically equation (58) for an arbitrary oriented fracture by computing the components of the aperture along two lines parallel to the x and y axes, $w_x(\mathbf{x})$ and $w_y(\mathbf{x})$, at every fracture point (Figure 3c). The discrete equation of the components of the aperture at the point (i, j) is approximated in a regular quadrilateral mesh as follows:

$$w_x(\mathbf{x}) \approx w_{x,i,j} = \sum_{k=i-a}^{k=i+b} u_{x,k,j} \frac{d_{k+1,j} - d_{k-1,j}}{2\delta_x} \delta_x, \tag{59}$$

and

$$w_y(\mathbf{x}) \approx w_{y,i,j} = \sum_{k=i-a}^{k=i+b} u_{y,i,k} \frac{d_{i,k+1} - d_{i,k-1}}{2\delta_y} \delta_y. \tag{60}$$

The aperture is given by the addition of the projection of $w_{x,i,j}$ and $w_{y,i,j}$ onto the normal to the fracture path

$$w_{i,j} = w_{x,i,j} \sin \beta_{i,j} + w_{y,i,j} \cos \beta_{i,j}. \tag{61}$$

The angle $\beta_{i,j}$, which defines the normal to the path at the cell (i, j), is computed through a curve fitted to the fracture domain.

The integral form of the conservation law (41) of the mechanics problem over an arbitrary control volume reads

$$\int_\Omega \nabla \cdot \boldsymbol{\sigma}' \mathrm{d}\Omega - \int_\Omega \alpha g(d) \nabla p \mathrm{d}\Omega + \int_\Omega p \nabla g(d) \mathrm{d}\Omega + \int_\Omega \mathbf{f} \mathrm{d}\Omega = 0. \tag{62}$$

Using the divergence theorem, the discrete equations for the displacements u and v for a given control volume (i, j) in a Cartesian grid are:

$$\begin{aligned}[\sigma'_{xx}]_{i+1/2,j} - [\sigma'_{xx}]_{i-1/2,j} + [\sigma'_{xy}]_{i,j+1/2} - [\sigma'_{xy}]_{i,j-1/2} + \\ - \alpha \left(p_{i+1/2,j} - p_{i-1/2,j}\right) \delta y - p_{i,j} \left[g(d)_{i+1/2,j} - g(d)_{i-1/2,j}\right] \delta y + f_x \delta x \delta y = 0,\end{aligned} \tag{63}$$

$$\begin{aligned}[\sigma'_{yx}]_{i+1/2,j} - [\sigma'_{yx}]_{i-1/2,j} + [\sigma'_{yy}]_{i,j+1/2} - [\sigma'_{yy}]_{i,j-1/2} + \\ - \alpha \left(p_{i,j+1/2} - p_{i,j-1/2}\right) \delta x - p_{i,j} \left[g(d)_{i,j+1/2} - g(d)_{i,j-1/2}\right] \delta x + f_y \delta x \delta y = 0.\end{aligned} \tag{64}$$

We approximate the stress fluxes at the interfaces with

$$\begin{aligned}[\sigma'_{xx}]_{i+1/2,j} = \left(\lambda_{i+1/2,j} + 2\mu_{i+1/2,j}\right) \frac{u_{i+1,j} - u_{i,j}}{\delta x} \delta y + \\ + \lambda_{i+1/2,j} \frac{v_{i+1,j+1} + v_{i,j+1} - v_{i+1,j-1} - v_{i,j-1}}{4\delta y} \delta y,\end{aligned} \tag{65}$$

$$\begin{aligned}[\sigma'_{yy}]_{i,j+1/2} = \left(\lambda_{i,j+1/2} + 2\mu_{i,j+1/2}\right) \frac{v_{i,j+1} - v_{i,j}}{\delta y} \delta x + \\ + \lambda_{i,j+1/2} \frac{u_{i+1,j+1} + u_{i+1,j} - u_{i-1,j+1} - u_{i-1,j}}{4\delta x} \delta x,\end{aligned} \tag{66}$$

$$[\sigma'_{xy}]_{i,j+1/2} = \mu_{i,j+1/2} \left(\frac{v_{i+1,j+1} + v_{i+1,j} - v_{i-1,j+1} - v_{i-1,j}}{4\delta x} + \frac{u_{i,j+1} - u_{i,j}}{\delta y} \right) \delta x, \tag{67}$$

$$[\sigma'_{yx}]_{i+1/2,j} = \mu_{i+1/2,j} \left(\frac{v_{i+1,j} - v_{i,j}}{\delta x} + \frac{u_{i+1,j+1} + u_{i,j+1} - u_{i+1,j-1} - u_{i,j-1}}{4\delta y} \right) \delta y, \tag{68}$$

and similar for the $[\cdot]_{i-1/2,j}$ and $[\cdot]_{i,j-1/2}$ interfaces. As above, the interface mechanical properties, λ and μ, are approximated using the harmonic mean. The Lamé constants for the hybrid formulation and plain strain state reads

$$\lambda_{i,j} = \frac{\nu g(d)_{i,j} E}{(1+\nu)(1-2\nu)}, \quad \mu_{i,j} = \frac{g(d)_{i,j} E}{2(1+\nu)}. \tag{69}$$

We approximate the pressure at the interfaces with the arithmetic mean

$$p_{i\pm1/2,j} = \frac{p_{i\pm1,j} + p_{i,j}}{2}, \quad p_{i,j\pm1/2} = \frac{p_{i,j\pm1} + p_{i,j}}{2}, \tag{70}$$

and similar for the degradation function, $g(d)$. Rearranging the expression (63), we arrive at

$$\begin{aligned}&\left(\lambda_{i+1/2,j} + 2\mu_{i+1/2,j}\right) \frac{\delta y}{\delta x} u_{i+1,j} + \mu_{i,j+1/2} \frac{\delta x}{\delta y} u_{i,j+1} + \mu_{i,j-1/2} \frac{\delta x}{\delta y} u_{i,j-1} \\ &- \left[\left(\lambda_{i-1/2,j} + \lambda_{i+1/2,j} + 2\mu_{i-1/2,j} + 2\mu_{i+1/2,j}\right) \frac{\delta y}{\delta x} + \left(\mu_{i,j-1/2} + \mu_{i,j+1/2}\right) \frac{\delta x}{\delta y} \right] u_{i,j} + \\ &+ \left(\lambda_{i-1/2,j} + 2\mu_{i-1/2,j}\right) \frac{\delta y}{\delta x} u_{i-1,j} + \frac{1}{4} \left(\lambda_{i+1/2,j} + \mu_{i,j+1/2}\right) v_{i+1,j+1} \\ &+ \frac{1}{4} \left(\mu_{i,j+1/2} - \mu_{i,j-1/2}\right) v_{i+1,j} - \frac{1}{4} \left(\lambda_{i+1/2,j} + \mu_{i,j-1/2}\right) v_{i+1,j-1} \\ &+ \frac{1}{4} \left(\lambda_{i+1/2,j} - \lambda_{i-1/2,j}\right) v_{i,j+1} + \frac{1}{4} \left(\lambda_{i-1/2,j} - \lambda_{i+1/2,j}\right) v_{i,j-1} \\ &- \frac{1}{4} \left(\lambda_{i-1/2,j} + \mu_{i,j+1/2}\right) v_{i-1,j+1} + \frac{1}{4} \left(\mu_{i,j-1/2} - \mu_{i,j+1/2}\right) v_{i-1,j} \\ &+ \frac{1}{4} \left(\lambda_{i-1/2,j} + \mu_{i,j-1/2}\right) v_{i-1,j-1} + \frac{\alpha \delta y}{2} \left(p_{i-1,j} - p_{i+1,j}\right) \\ &+ \left[g(d)_{i-1/2,j} - g(d)_{i+1/2,j}\right] \delta y p_{i,j} = f_x \delta x \delta y,\end{aligned} \tag{71}$$

and for the expression (64) at

$$\begin{aligned}
&\frac{1}{4}\left(\lambda_{i,j+1/2}+\mu_{i+1/2,j}\right)u_{i+1,j+1}+\frac{1}{4}\left(\lambda_{i,j+1/2}-\lambda_{i,j-1/2}\right)u_{i+1,j}\\
&-\frac{1}{4}\left(\lambda_{i,j-1/2}+\mu_{i+1/2,j}\right)u_{i+1,j-1}+\frac{1}{4}\left(\mu_{i+1/2,j}-\mu_{i-1/2,j}\right)u_{i,j+1}\\
&+\frac{1}{4}\left(\mu_{i-1/2,j}-\mu_{i+1/2,j}\right)u_{i,j-1}-\frac{1}{4}\left(\mu_{i-1/2,j}+\lambda_{i,j+1/2}\right)u_{i-1,j+1}\\
&+\frac{1}{4}\left(\lambda_{i,j-1/2}-\lambda_{i,j+1/2}\right)u_{i-1,j}+\frac{1}{4}\left(\mu_{i-1/2,j}+\lambda_{i,j-1/2}\right)u_{i-1,j-1}\\
&+\left(\lambda_{i,j+1/2}+2\mu_{i,j+1/2}\right)\frac{\delta x}{\delta y}v_{i,j+1}+\mu_{i+1/2,j}\frac{\delta y}{\delta x}v_{i+1,j}+\mu_{i-1/2,j}\frac{\delta y}{\delta x}v_{i-1,j}\\
&-\left[\left(\lambda_{i,j+1/2}+2\mu_{i,j+1/2}+\lambda_{i,j-1/2}+2\mu_{i,j-1/2}\right)\frac{\delta x}{\delta y}+\left(\mu_{i-1/2,j}+\mu_{i+1/2,j}\right)\frac{\delta y}{\delta x}\right]v_{i,j}\\
&+\left(\lambda_{i,j-1/2}+2\mu_{i,j-1/2}\right)\frac{\delta x}{\delta y}v_{i,j-1}+\frac{\alpha\delta x}{2}\left(p_{i,j-1}-p_{i,j+1}\right)\\
&+\left[g(d)_{i,j-1/2}-g(d)_{i,j+1/2}\right]\delta x p_{i,j}=f_y\delta x\delta y.
\end{aligned}\tag{72}$$

The updated pressure, displacements, and fracture-matrix flux at the next time level $n+1$ are obtained after solving the linear system of equations

$$\mathbf{U}^{n+1}=\mathbf{K}_{\text{full}}^{-1}\mathbf{R}^{n},\tag{73}$$

where the vectors of unknowns **U** include cell pressures, displacements, and, if exists, fluid flow between domains

$$\mathbf{U}^{n+1}=\begin{pmatrix}\mathbf{p}^{n+1}\\ \mathbf{q}^{n+1}\\ \mathbf{u}^{n+1}\end{pmatrix}=\begin{pmatrix}p_{(1,1)}^{n+1}\\ \vdots\\ p_{(N,M)}^{n+1}\\ q_{1}^{n+1}\\ \vdots\\ q_{K}^{n+1}\\ u_{(1,1)}^{n+1}\\ \vdots\\ u_{(N,M)}^{n+1}\\ v_{(1,1)}^{n+1}\\ \vdots\\ v_{(N,M)}^{n+1}\end{pmatrix}\tag{74}$$

where we recall $q^{n+1}=Q_{mf}^{n+1}$, and the system matrix is a 4×4 block matrix

$$\mathbf{K}_{\text{full}}=\begin{pmatrix}\mathbf{K}_{pp} & \mathbf{K}_{pq} & \mathbf{K}_{pu} & \mathbf{K}_{pv}\\ \mathbf{K}_{qp} & \mathbf{K}_{qq} & \mathbf{K}_{qu} & \mathbf{K}_{qv}\\ \mathbf{K}_{up} & 0 & \mathbf{K}_{uu} & \mathbf{K}_{uv}\\ \mathbf{K}_{vp} & 0 & \mathbf{K}_{vu} & \mathbf{K}_{vv}\end{pmatrix}\tag{75}$$

and the source vector is

$$\mathbf{R}^{n}=\begin{pmatrix}\mathbf{R}_{p}^{n}\\ \mathbf{R}_{q}^{n}\\ \mathbf{R}_{u}^{n}\\ \mathbf{R}_{v}^{n}\end{pmatrix}.\tag{76}$$

The coefficients of the p-blocks, $\mathbf{K}_{pp},\ldots,\mathbf{K}_{pv}$, are given by equation (50); the q-blocks, $\mathbf{K}_{qp},\ldots,\mathbf{K}_{qv}$, by equation (56); the u-displacement blocks, $\mathbf{K}_{up},\ldots,\mathbf{K}_{uv}$, by equation (71); and the v-displacement blocks, $\mathbf{K}_{up},\ldots,\mathbf{K}_{uv}$, by equation (72). The corresponding coefficients of the source vector are also given by the same equations.

2.4.2. Numerical Implementation of the Phase Field Equation

The integral form of the phase field equation (42) over an arbitrary control volume Ω reads

$$\int_{\Omega}\left(\frac{g_c}{\ell}+2H^{+}\right)d\mathrm{d}\Omega+\int_{\Omega}g_c\ell\nabla^2 d\mathrm{d}\Omega-\int_{\Omega}2H^{+}\mathrm{d}\Omega=0. \tag{77}$$

Using the divergence theorem, the above expression is rewritten as

$$\int_{\Omega}\left(\frac{g_c}{\ell}+2H^{+}\right)d\mathrm{d}\Omega+\int_{\partial\Omega}g_c\ell\nabla d\mathrm{d}\partial\Omega-\int_{\Omega}2H^{+}\mathrm{d}\Omega=0. \tag{78}$$

The discrete equation for the phase field problem is, for a given control volume (i,j) in a regular Cartesian grid,

$$\begin{aligned}\left(\frac{g_c}{\ell}+2H^{+}\right)d_{i,j}\delta x\delta y+\left[-g_c\ell\frac{\partial d}{\partial x}\right]_{i+1/2,j}+\left[g_c\ell\frac{\partial d}{\partial x}\right]_{i-1/2,j}\\+\left[-g_c\ell\frac{\partial d}{\partial y}\right]_{i,j+1/2}+\left[g_c\ell\frac{\partial d}{\partial y}\right]_{i,j-1/2}-2H^{+}\delta x\delta y=0.\end{aligned} \tag{79}$$

The fully discrete equation is given by

$$\begin{aligned}\left(\frac{g_c}{\ell}+2H^{+}\right)d_{i,j}\delta x\delta y-g_{c,i+1/2,j}\ell\left(\frac{d_{i+1,j}-d_{i,j}}{\delta x}\right)\delta y+g_{c,i-1/2,j}\ell\left(\frac{d_{i,j}-d_{i-1,j}}{\delta x}\right)\delta y\\-g_{c,i,j+1/2}\ell\left(\frac{d_{i,j+1}-d_{i,j}}{\delta y}\right)\delta x+g_{c,i,j-1/2}\ell\left(\frac{d_{i,j}-d_{i,j-1}}{\delta y}\right)\delta x-2H^{+}\delta x\delta y=0.\end{aligned} \tag{80}$$

The interface critical energy release rate is computed, as in the previous equations, with the harmonic mean. Rearranging the above expression, we arrive at

$$\begin{aligned}&\left[\left(\frac{g_c}{\ell}+2H^{+}\right)\delta x\delta y+\left(g_{c,i+1/2,j}+g_{c,i-1/2,j}\right)\ell\frac{\delta y}{\delta x}+\left(g_{c,i,j+1/2}+g_{c,i,j-1/2}\right)\ell\frac{\delta x}{\delta y}\right]d_{i,j}\\&-g_{c,i+1/2,j}\ell\frac{\delta y}{\delta x}d_{i+1,j}-g_{c,i-1/2,j}\ell\frac{\delta y}{\delta x}d_{i-1,j}-g_{c,i,j+1/2}\ell\frac{\delta x}{\delta y}d_{i,j+1}\\&-g_{c,i,j-1/2}\ell\frac{\delta x}{\delta y}d_{i,j-1}=2H^{+}\delta x\delta y.\end{aligned} \tag{81}$$

The updated phase field is obtained after solving the linear system of equations

$$\mathbf{D}=\mathbf{K}^{-1}\mathbf{R}_d, \tag{82}$$

where the vectors of unknowns $\mathbf{D}$ include cell phase fields

$$\mathbf{D}=\begin{pmatrix}d_{(1,1)}\\d_{(2,1)}\\\vdots\\d_{(N,M)}\end{pmatrix}. \tag{83}$$

The coefficients of the system matrix $\mathbf{K}$ and the source vector $\mathbf{R}_d$ are given by equation (81).

2.4.3. Tracking Algorithm of the Fracture

In our Cartesian grid, the 1-D fracture domain, Ω_R, is composed by a set of 0 and $\pi/2$ radians segments. It is updated by adding at each time step a set of segments that links the previous fracture tip with the new one. We explain our strategy through Figure 3. At time step $n+1$, the displacement field $\mathbf{u}^{n+1}$ and the phase field d^{n+1} are known, as well as the fracture path at the previous time step, Ω_F^n. We determine the fracture domain at the time step $n+1$ through an iterative process that compromises two steps.

In the first step of the kth iteration, we group in Ω_{tip}^k the four neighboring cells surrounding the current tip, $\mathbf{x}_{\mathrm{tip},i,j}^{n,k-1}$, except the ones that are already part of the fracture. Out of those candidate neighboring cells, we retain the ones for which the phase field variable exceeds a prescribed threshold value, d_f. The set of candidates that could become the new fracture tip after applying this first step is

$$\Omega_{\mathrm{tip}}^k=\left\{\mathbf{x}_{\mathrm{tip},I=i\pm1,J=j\pm1}^{n,k-1}\,I\neq J\ /\ \mathbf{x}_{I,J}\notin\Omega_F^n\ ,\ d_{I,J}^{n+1}\geq d_f\right\}. \tag{84}$$

In the second step, we determine the direction of propagation of the fracture by selecting the new fracture tip among the above set of candidates. The new tip, $\mathbf{x}^{n,k}_{\text{tip},i,j'}$ is done by determining the direction where the gradient of d is minimum:

$$\mathbf{x}^{n,k}_{\text{tip},i,j} = \min_{\mathbf{x}\in\Omega^k_{\text{tip}}} \nabla d(\mathbf{x}) \cdot \mathbf{x}, \tag{85}$$

where $\mathbf{x}$ is the versor direction. For example, in Figure 3b the fracture tip would propagate to the next cell in the vertical direction. The iteration process is repeated K times until $\Omega^k_{\text{tip}} = \varnothing$. The new fracture tip is then $\mathbf{x}^{n+1}_{\text{tip},i,j} = \mathbf{x}^{n,K}_{\text{tip},i,j}$. A limitation of our tracking algorithm is related to branching. Our algorithm is unable to capture branching and, consequently, is limited to track a single fracture.

To avoid abrupt changes in the direction of the normal to the fracture trajectory we fit a function to the fracture domain at every time step. We computed the normal direction to the fracture path through this function. The function can be defined by splines, piecewise functions, Fourier series, or polynomials, for example. For our particular problem where fractures describe smooth trajectories, we choose a polynomial with shape $y = a_1 + a_2x + a_3x^{1.5}$. Coefficients a_i are determined by the least squares method.

3. Benchmark Analytical Model and Code Verification

The performance of the numerical model is tested against two benchmarks. The simple first test of the poroelastic model is an analytic solution of the Biot poroelasticity equation in a 2-D domain derived from Barry and Mercer (1999). The second benchmark is the Sneddon analytical solution of a pressurized fracture with constant length located in a 2-D infinite elastic domain (Sneddon, 1946).

3.1. Analytical Solution of the Poroelasticity Equations

Analytical solutions of the Biot model are available under the standard linear poroelastic assumptions: homogeneous and isotropic material with constant medium permeability, linear stress-strain dependence and infinitesimal strains, incompressible fluid and solid materials, and constant temperature.

Under these assumptions, we consider a 2-D rectangular domain $\Omega = (a, b)^2$ with a point source $q(x, y, t)$ at (x_0, y_0) (see Figure 4). The boundary conditions for flow are zero pressure, whereas for displacements are $u = 0$ and $\partial v/\partial y = 0$ on $y = 0$ and $y = b$; and $v = 0$, $\partial u/\partial x = 0$ on $x = 0$ and $x = a$. The imposed flow rate is

$$q(x, y, t) = \beta\delta(x - x_0)\delta(y - y_0)e^{\omega t}, \tag{86}$$

where β [T^{-1}] and ω [T^{-1}] are constants, and δ is the Dirac delta function. The analytical solution is obtained by applying Laplace transforms and Fourier expansions and reads

$$u(x, y, t) = \frac{4}{ab}\sum_{q=1}^{\infty}\sum_{n=1}^{\infty}\bar{u}(n, q, t)\cos(\varphi_n x)\sin(\varphi_q y), \tag{87}$$

$$v(x, y, t) = \frac{4}{ab}\sum_{q=1}^{\infty}\sum_{n=1}^{\infty}\bar{v}(n, q, t)\cos(\varphi_n x)\sin(\varphi_q y), \tag{88}$$

$$p(x, y, t) = -\frac{4}{ab}\sum_{q=1}^{\infty}\sum_{n=1}^{\infty}\bar{p}(n, q, t)\cos(\varphi_n x)\sin(\varphi_q y), \tag{89}$$

where

$$\bar{u}(n, q, t) = \frac{1}{\lambda + 2\mu}\frac{\varphi_n}{\hat{\varphi}}\bar{p}(n, q, t), \quad \bar{v}(n, q, t) = \frac{1}{\lambda + 2\mu}\frac{\varphi_q}{\hat{\varphi}}\bar{p}(n, q, t), \tag{90}$$

λ and μ are the Lamé constants,

$$\bar{p}(n, q, t) = -\frac{\beta}{k^*}\frac{\sin(\varphi_n x_0)\sin(\varphi_q y_0)}{\hat{\varphi} + \omega}\left(e^{\omega t} - e^{-\hat{\varphi}t}\right), \tag{91}$$

and $k^* = \kappa/\mu_f$. Finally, we define

$$\varphi_n = \frac{n\pi}{a}, \quad \varphi_q = \frac{q\pi}{b}, \quad \hat{\varphi} = \varphi_n^2 + \varphi_q^2. \tag{92}$$

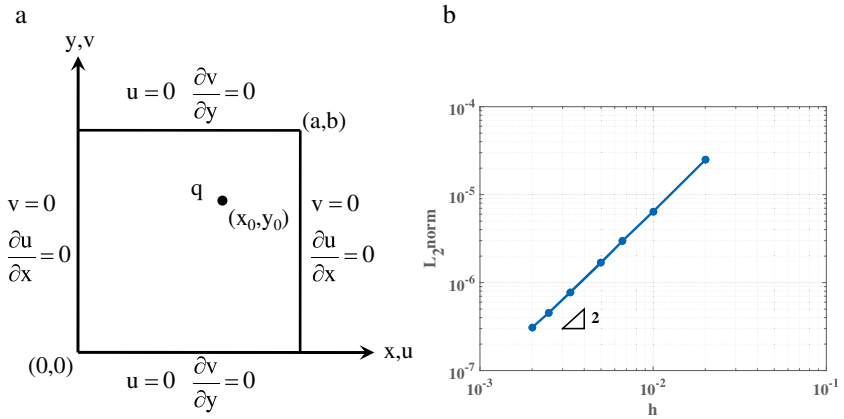

Figure 4. Poroelastic benchmark model. (a) Model setup for the verification with injection point at (x_0, y_0). (b) Testing the grid convergence, log-log scale plot of the L_2 error norm measure for the u displacements, plotted against the mesh size h. As expected, the displacements converge quadratically.

The discrepancy between the analytical and the numerical models is measured computing the L_2 error norm, given by

$$L_2 = \|V^{\text{ex}} - V^{\text{num}}\|_2 = \left\{ \sum_{i=1}^{N_i} \sum_{j=1}^{N_j} \int_{\Omega} \left(V_{i,j}^{\text{ex}} - V_{i,j}^{\text{num}} \right)^2 d\Omega \right\}^{1/2}, \tag{93}$$

where $V_{i,j}^{\text{ex}}$ is the exact value of the variable at location (i, j) and $V_{i,j}^{\text{num}}$ is its value computed with the numerical model.

The numerical model is applied to the domain depicted in Figure 4a, with unit length and hydromechanical properties: $E = 1$ [$\text{ML}^{-1}\text{T}^{-2}$], $\nu = 0.25$, $k^* = 1$ [$\text{M}^{-1}\text{L}^3\text{T}$], $\alpha = 1$, and $S = 0$ [M^{-1}LT^2]. Fluid is injected at constant rate $q = 1$ [T^{-1}] at location (0.75 [L], 0.75 [L]). We test the grid convergence of the base poroelastic solver by discretizing the domain with several mesh sizes and computing the L_2 norm, equation (93). We adopt a finite volume scheme on a regular quadrilateral mesh for the spatial discretization and a Backward Euler scheme for the time integration. Pressure and displacement fields are solved with a fully coupled scheme. The results for the u displacements are depicted in Figure 4b in log-log scale. The displacements converge quadratically, as expected from the order of the numerical scheme, second order.

3.2. Sneddon Analytical Solution for a Pressurized Fracture

The second benchmark is based on the analytical solutions obtained by Sneddon (1946). Sneddon considered an infinite 2-D elastic domain with a Griffith fracture of constant length $2c$ centered at the origin of the Cartesian coordinate system, and whose axis is aligned with the x axis. The elastic material is assumed to be homogeneous and isotropic, with linear stress-strain dependence, isothermal conditions, and plane and infinitesimal strains. Under these assumptions, the aperture of the fracture under constant pressure applied to its edges is given by

$$w(x, 0) = \frac{4(1 - \nu^2)pc}{E} \sqrt{1 - \frac{x^2}{c^2}}. \tag{94}$$

This simple model allows us to validate equation (24), where pressure forces are accounted for as body forces in the phase field formulation.

We consider a 2-D squared domain of length 4 [L] with mechanical properties: $E = 1$ [$\text{ML}^{-1}\text{T}^{-2}$], $\nu = 0.25$, $g_c = 1.80 \times 10^{-10}$ [MT^{-2}], and $\ell = 0.015$ [L]. The boundary conditions are zero displacements. The fracture has a length of 1 [L], and it is introduced by setting such a large value for H^+ in the damaged area that the value of the phase field is very close to 1 in the fracture (Figure 5a). The applied pressure is 10^{-4} [$\text{ML}^{-1}\text{T}^{-2}$], and the aperture of the fracture is computed through equation (41).

We plot the vertical (normal to the fracture) displacements in Figure 5b. By using these displacements and the phase field variable, we compute the aperture, which is plotted in Figure 5c for several mesh sizes ranging

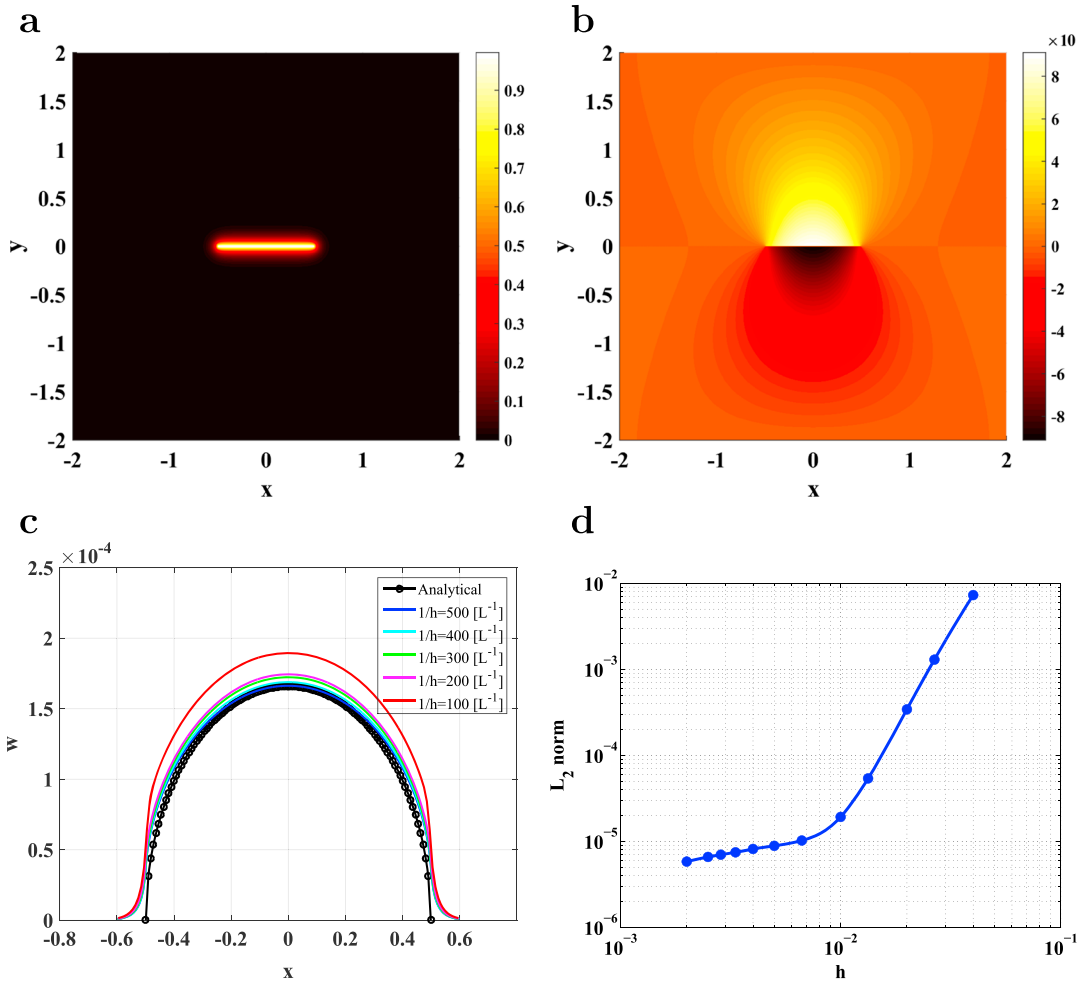

Figure 5. Sneddon benchmark model. (a) Initial fracture: map of phase field (damage) variable d. Model results: (b) contour plot of normal displacements, (c) fracture profiles for the analytical solution and the numerical model with mesh sizes ranging from 1/100 to 1/500 [L], and (d) L_2 error norm for the fracture aperture against the mesh size h. The phase field model results agree well with the analytical solution except near the tips, where the phase field model introduces a smearing effect due to the regularization of the fracture surface.

from 1/70 to 1/500 [L]. In the same figure we depict the aperture computed with the analytical solution. We plot the L_2 error norm of the fracture aperture against the mesh size in log-log scale in Figure 5d. The numerical results converge to the analytical solution as the element size decreases. The aperture converges quartically for the largest mesh sizes up to $h = 1/100$ [L]. For smaller sizes, the convergence order is lower than one. The convergence order of the aperture differs from the order of the numerical scheme—equal to 2—since the aperture is a variable computed from the solution of the numerical model. These results suggest that a good choice of the mesh size is $h = 1/400 = 2.5 \times 10^{-3}$ [L]. The accuracy of the numerical solution, in terms of the root-mean-square error, is 6.6×10^{-6} [L] for this size.

The numerical models agree well with the analytical solution except near the fracture tips, where the phase field model does not match the exact solution due to the smearing effect introduced by the regularization of the fracture.

4. Numerical Assessment of the Phase Field Approach to Hydraulic Fracturing

4.1. The Propagation of a Fracture in the Quarter Five-Spot Problem

To test the potential of the proposed methodology to describe realistic injection scenarios, we consider the case of the propagation of a hydraulic fracture in the quarter five-spot configuration of injection and production wells (Figure 6). Due to its practical importance in enhanced oil recovery, this arrangement has served

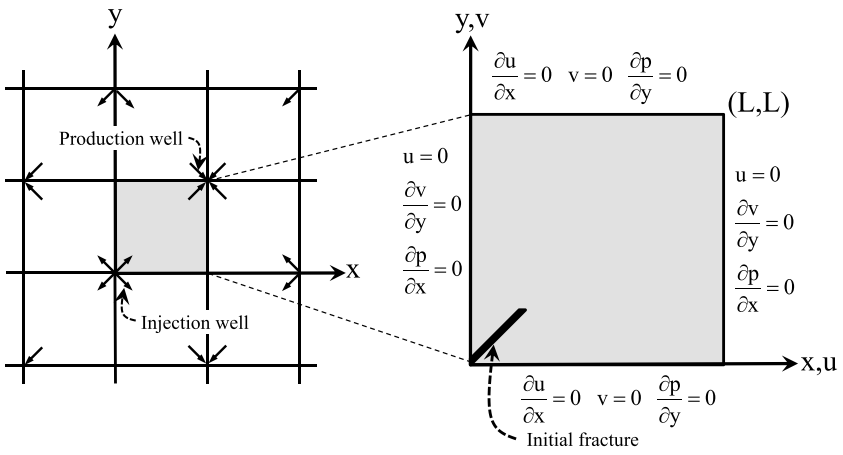

Figure 6. Schematic diagram of the quarter five-spot configuration. Our computational domain is the shaded area.

as the paradigm configuration in many porous media problems for exploring miscible and immiscible fluid displacements (Christie & Blunt, 2001; Coats, 1982; Lajeunesse et al., 1999; Lie & Juanes, 2005; Riaz & Meiburg, 2003; Russell & Wheeler, 1983; Zhang et al., 1997). We model fracturing induced by injection at constant flow rate at the bottom-left corner of a two-dimensional square domain of length L, while fluid is produced at the top-right corner at constant pressure. An initial straight fracture of length $0.15L$ is aligned along the domain diagonal. This fracture is introduced as a region with a large value of the local history field of maximum positive energy such that the computed phase field was close to the broken state. In that way, a consistent initial condition is guaranteed. The poroelastic medium is assumed to be initially homogeneous and isotropic, with constant permeability, linear stress-strain dependence, and infinitesimal planar strains. Symmetry boundary conditions are imposed; that is, $\partial u/\partial x = 0$, $v = 0$, $\partial p/\partial y = 0$ on $y = 0$ and $y = 1$, and $u = 0$, $\partial v/\partial y = 0$, $\partial p/\partial x = 0$ on $x = 0$ and $x = L$.

The mechanical and hydraulic properties of the media and the fluid are listed in Table 1. The values correspond to sandstone saturated with water, and water is also the injected fluid. The dimensional analysis of the governing equations renders five dimensionless parameters:

$$\pi_1 = \frac{g_c}{EL}, \quad \pi_2 = \frac{M}{E}, \quad \pi_3 = \frac{\mu_f k^*}{L^2}, \quad \pi_4 = \frac{Q}{Ek^*}, \quad \pi_5 = \frac{tEk^*}{L^2}, \tag{95}$$

where $k^* = \kappa/\mu_f$ is the ratio between the medium intrinsic permeability and the fluid dynamic viscosity. Since we consider plane-strain conditions, the previous magnitudes are measured per unit thickness of solid. Taking E, L, and k^* as reference magnitudes, we compute the dimensionless parameters shown in Table 1.

With this test we aim at assessing the physical consistency and convergence properties of phase field models and corresponding numerical discretizations. For a given injection flow rate above the breakdown threshold, we expect that the fracture will propagate a certain distance, reaching a steady state length and flow configuration. The arrest of fracture propagation is expected to occur due to the poroelastic coupling. We choose

Table 1
Model Parameters for the Quarter Five-Spot Configuration

Parameter	Name	Dimensional value	Dimensionless value
E	Young modulus	17 GPa	1
L	Length of domain	40 m	1
$k^* = \kappa/\mu_f$	Ratio permeability to viscosity	1×10^{-11} m^2 Pa^{-1} s^{-1}	1
g_c	Griffith critical energy release rate	120 J m^{-2}	1.8×10^{-10}
M	Biot modulus	53.7 MPa	3.2×10^{-3}
μ_f	Dynamic viscosity	10^{-3} Pa s	6.6×10^{-18}
c_f	Fluid compressibility	4.5×10^{-10} Pa^{-1}	7.65
ν	Poisson ratio		0.25
α	Biot coefficient		0.90

the final fracture length as the key model output to be analyzed. The question is, then, how this length depends on hydromechanical and injection parameters, and whether it is robust when the grid, or the length scale parameter, ℓ, change. In summary, we assess whether the fracture patterns observed are robust and physically relevant, rather than grid controlled in an ill-posed problem. We have also conducted a parametric study to evaluate the physical consistency of the model.

4.2. Observed Fracture Propagation Patterns

By varying the imposed injection flow rate, we conduct multiple experiments of fracture propagation in the quarter five-spot problem. The injection-driven fracture propagation is resolved in time until a steady state is reached, where pressures, mechanical deformations, and damage (phase field) variables do not change in time further. We consider that the steady state has been reached when the convergence criteria fulfill. The criteria refer to $\left|(s_i - s_{i-1})/s_i\right| < T$, where s_i is the value of the considered variable s at time i and T is the relative tolerance. We adopt $T = 10^{-3}$. For given hydromechanical properties, the steady state fracture length depends on the injection rate, and three distinctive patterns arise: (1) for low enough injection rates, the initial fracture does not propagate; (2) for a given injection flow rate above a breakdown threshold, the initial fracture propagates and a steady state fracture length is reached, the steady state length increases with injection rate. and, in the absence of heterogeneity or disorder, the fracture propagates along the diagonal from the injection to producing well; and (3) for high rates, the fracture branches near the production well, where compressive stresses concentrate. Figure 7 illustrates the three fracture patterns, along with the corresponding evolution of the injection pressure and flow rates. In what follows, we describe and analyze patterns that we observe in the simulations.

Fractures propagate due to the pressure gradient generated at the interface between the fracture and the porous medium, which results in strain concentration at fracture tips and induces damage, that is, increases the phase field variable. The magnitude of the strains depends on the pressure gradient, which increases with the injection flow rate for constant hydromechanical properties. For relatively small injection rates, the pressure gradient is not large enough to propagate the fracture (Figure 7a). Under this situation, the injection pressure and production flow rate increase with time up to constant values (Figure 7a).

The second pattern corresponds to injection flow rates for which the fracture propagates following a straight path and reaches a steady state length. That evolution is depicted in Figure 7b, where the dimensionless injection rate is $q = 5.0 \times 10^{-5}$. The production flow rate presents a similar evolution to the previous case, but the pressure evolution has a distinctive feature: an initial steep buildup up to the point where the fracture starts to grow, followed by a sudden decrease due to the propagation of the fracture. Afterward, the pressure continues to increase because of the nature of the hydraulic boundary conditions, zero flux, up to a steady state is reached. The leaked fluid from the fracture makes the pressure in the poroelastic medium increase, but the fluid pressure inside the fracture is not high enough and fracture propagation stops.

The last pattern corresponds to fractures driven by high ratios of q to k^*. In such cases, fractures branch near the top-corner production well (Figure 7c). This pattern emerges due to the combination of the fracture propagation velocity and the poroelastic effect. The high propagation velocity of the fracture does not allow to reach the steady state when the fracture is close to the production well. Due to the poroelastic effect, compressive stresses in the vicinity of the production well are generated as the production flow increases and the propagation stops. Afterward, if the fluid pressure is high enough, branching occurs. The pressure evolution is also characterized by a sudden drop when the fracture starts to propagate.

To test the robustness of branching with respect to the grid size and d value threshold, we conduct a mesh refinement and threshold study. We study the presence of branching, as well as the fracture length at which branching occurs, L_b. We confirm that branching is independent of the d value threshold and mesh size. For a given dimensionless flow rate of 5×10^{-4} without confinement, branching occurs for increasingly four d values of the threshold ranging from 0.80 to 0.95, insets of Figure 8a, as well as for increasingly fine seven mesh sizes, from 1/100 to 1/700, insets of Figure 8b.

The steady state fracture length at which branching occurs is not independent of d_f. The length decreases for increasing d value threshold. This is to be expected since larger strains are required to propagate the fracture as the threshold increases, Figure 8a. Nevertheless, L_b is grid independent: the steady state length converges for increasingly mesh size, Figure 8b.

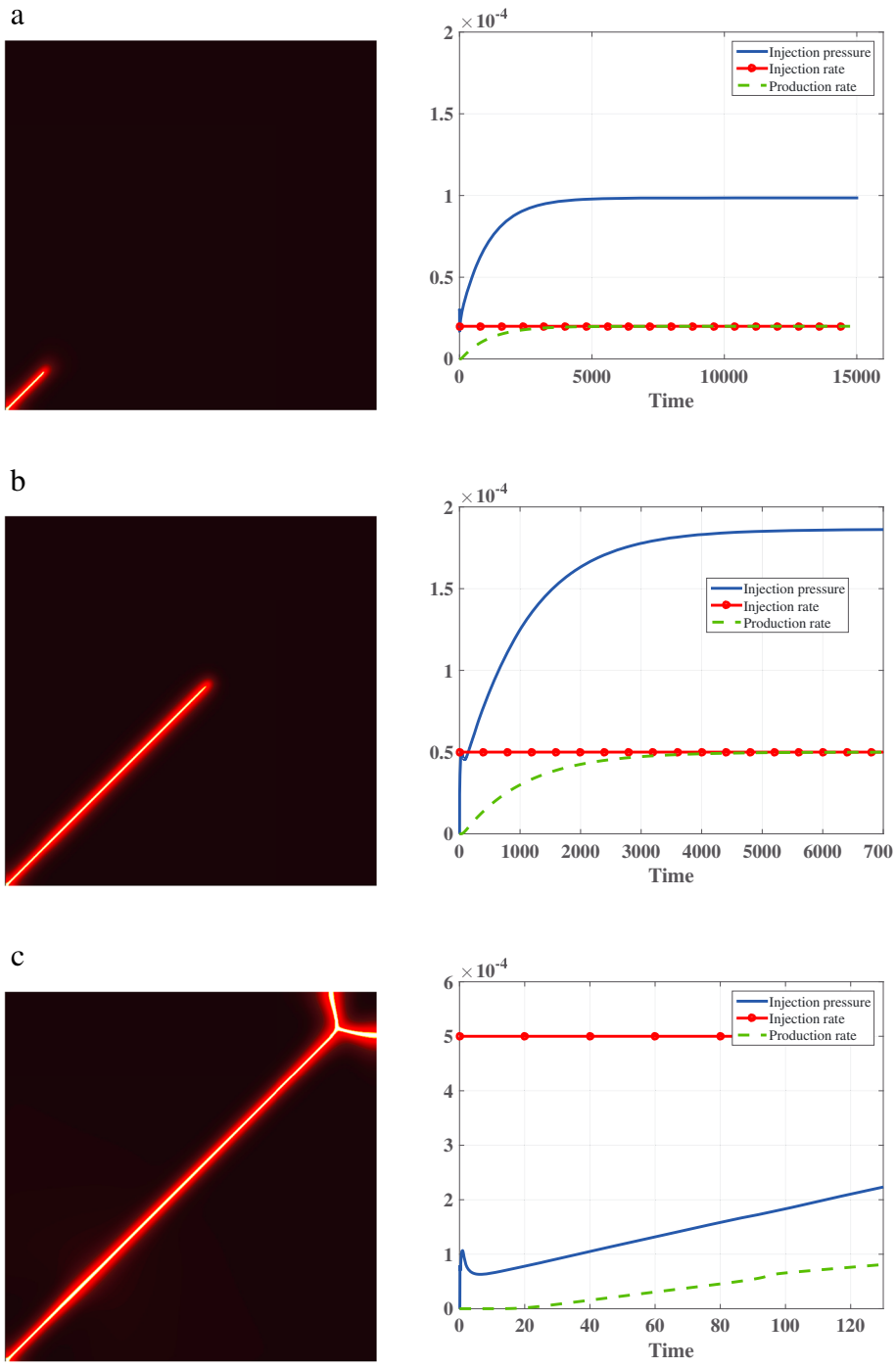

Figure 7. Steady state fracture patterns in the quarter five-spot configuration: phase field variable (left) and injection pressure evolution (right). (a) An initial fracture does not propagate for low enough injection rate; here $q = 2 \times 10^{-5}$. (b) For intermediate flow rates, an initial fracture grows until it reaches a steady state length; here $q = 5 \times 10^{-5}$. (c) For large enough flow rates, an initial fracture grows until it bifurcates near the production well, where compressive stresses dominate; here $q = 5 \times 10^{-4}$.

The permeability of the poroelastic medium has a direct influence on the leak-off flow rate from the fracture to the medium. We plot the evolution of the leak-off and storage flow rates in Figure 9a. The sum of both rates equals the injection rate, $q = 5.0 \times 10^{-4}$. Before the fracture begins to propagate, the pressure of the fluid inside the fracture rises, inducing an increase in the leak-off rate. Once the propagation starts, the fluid pressure suddenly drops and the leak-off rate decreases. Afterward, both variables (pressure and leak-off rate)

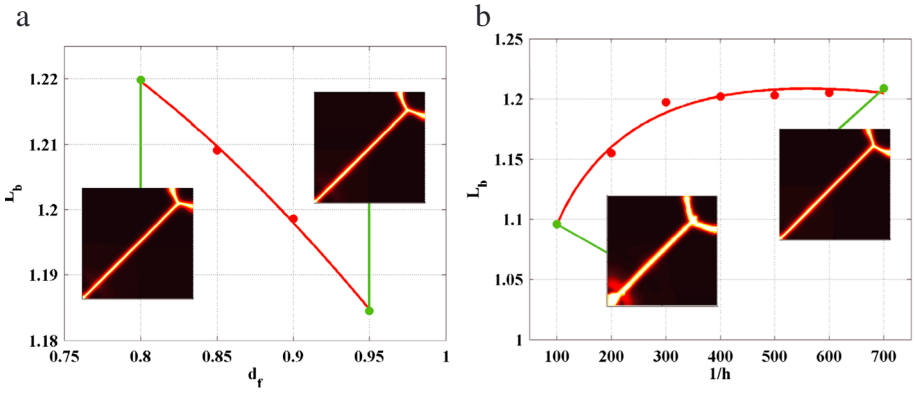

Figure 8. Convergence study for branching. The dimensionless flow rate is 5×10^{-4} without confinement. (a) We plot the steady state fracture length at the branching point, L_b, for several d value threshold, d_f. The steady state length decreases for increasing d value threshold. The branching is robust with respect to the selection of the threshold. (b) We depict the steady state fracture length at the branching point for several mesh sizes with $d_f = 0.90$. The model results are grid independent; the steady state length converges for increasingly fine mesh sized. The branching is also robust with respect to the mesh size.

increase with time, although the leak-off flow rate quickly grows up to a value close to the injection rate. The pressure distribution inside the fracture is shown in Figure 9b at three different times. The pressure is virtually uniform along the fracture during the entire simulation.

The high leak-off ratio indicates that most of the fluid is stored in the porous medium. Moreover, the uniform pressure along the fracture means that the viscous dissipation is negligible compared to the energy expended in fracturing the solid. Both phenomena indicate that the fracture propagates in the leak-off toughness dominated regime.

We depict the contour plots of pressure and phase field variables for the dimensionless injection flow rates $q = 5.0 \times 10^{-5}$ and $q = 5.0 \times 10^{-4}$ in Figures 10a and 10b, respectively, at two given times when both fractures have the same length. The maximum dimensionless pressure in both simulations is approximately 6×10^{-5}, but the distribution patterns are very different. The pressure field in the simulation with $q = 5.0 \times 10^{-5}$ (Figure 10a) is similar to the steady state pattern since the fracture propagation velocity is slow enough to allow the pressure to diffuse across the porous solid. The stationary fracture length and pressure fields are reached approximately at the same time, as can be seen from the right plot of Figure 7b, where the injection and production flow rates are coincident at time 4,000, when the stationary fracture length is also reached.

The pressure field pattern in the simulation with $q = 5.0 \times 10^{-4}$ (Figure 10b) is markedly different. The fracture propagates at such high velocity that the pressure has no time to diffuse through the medium, and it

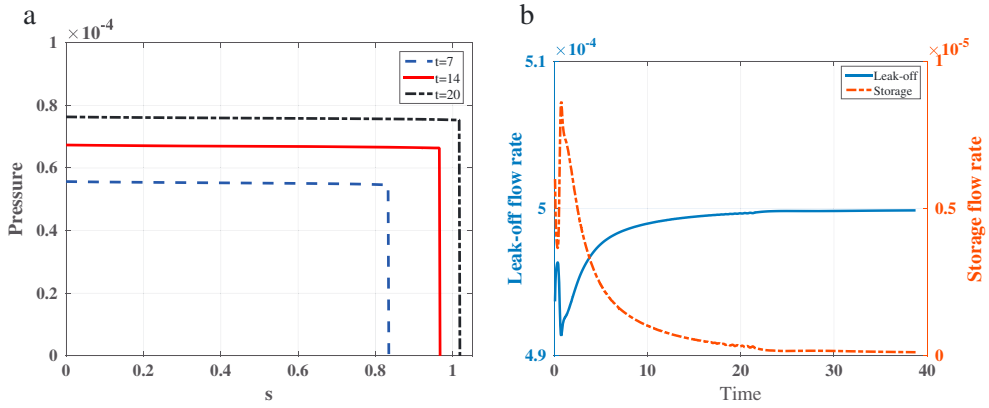

Figure 9. The permeability of the poroelastic medium has a direct influence on the leak-off flow rate from the fracture into the medium. (a) Evolution of the leak-off and storage flow rates. The sum of both rates equals the total injection rate, $q = 5 \times 10^{-4}$, which is constant in time. (b) Fluid pressure along the fracture at three time steps.

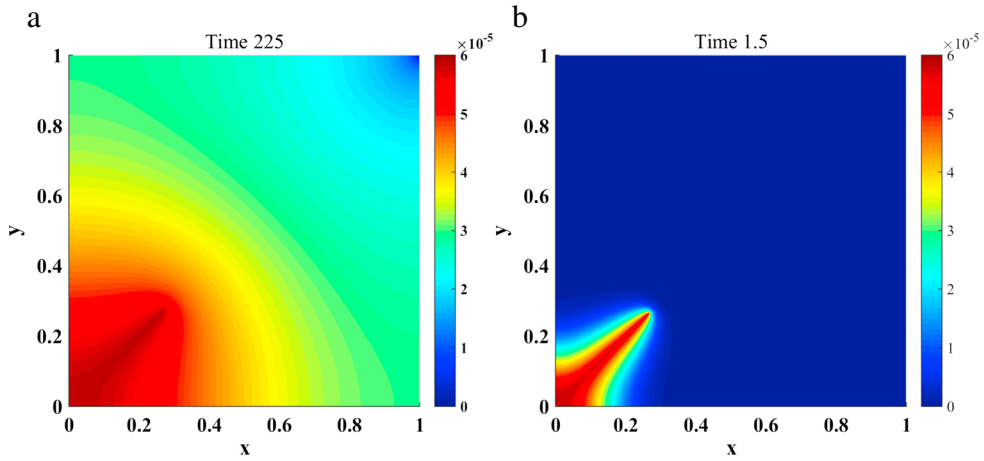

Figure 10. Hydraulic fractures propagate in the quarter five-spot configuration, reaching a final steady state length. Here we show maps of pressure field for (a) $q = 5 \times 10^{-5}$, and (b) $q = 5 \times 10^{-4}$. The dimensionless length of both fractures is 0.40. The pressure field in (a) is similar to the steady state pattern since the fracture propagation velocity is slow enough to allow the pressure to diffuse across the porous solid. Instead, the fracture propagates at such high velocity in (b) that the pressure has no time to diffuse through the medium, and it only changes in a small region around the damaged zone.

only changes in a small region around the damaged zone. The stationary fracture length is reached much earlier than the stationary pressure distribution, as shown in Figure 7c, where at dimensionless time 100 the stationary length occurs, but the production flow rate is 5 times lower than the injection rate.

4.3. Convergence Study on Phase Field Fracture Models

To test the grid convergence and grid independence of our model results, we conduct a mesh refinement study. In particular, we study the effect of mesh size over the final fracture length without confining strains and over the fracture path and aperture when confining strains are applied. We confirm that the model results are grid independent. For a fixed dimensionless injection flow rate of $q = 5 \times 10^{-5}$, the steady state lengths of the fracture converge for increasingly seven mesh sizes, from 1/100 up to 1/700 (Figure 11). The shortest dimensionless fracture length, 0.71, is computed with the coarsest dimensionless mesh size, 1/100. As the mesh is refined, the fracture length increases.

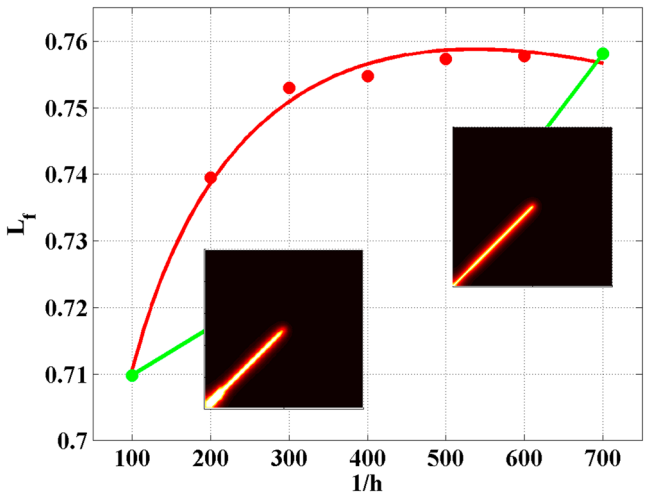

Figure 11. Effect of the mesh size on the steady state fracture length in the quarter five-spot configuration. The dimensionless flow injection rate is $q = 5 \times 10^{-5}$. The model results are grid independent: for a fixed dimensionless injection rate, the steady state fracture length converges for increasingly fine mesh sizes.

We also conduct a convergence study on a crack that propagates describing a curved path. For a far field displacement parallel to the y axis that under drained conditions produces confining strains $\varepsilon_{yy} = 1.25 \times 10^{-5}$ and $\varepsilon_{xx} = \varepsilon_{xy} = 0$ and a fixed dimensionless injection flow rate of $q = 5 \times 10^{-5}$, the steady state fracture path describes a curve, Figure 12a. We quantify the robustness of these trajectories by computing the root-mean-square deviation, S_r, of the simulated fracture paths with respect to the trajectory obtained using the smallest mesh size, Figure 12b. The difference between predicted trajectories decreases as the grid is refined, as it remains relatively small even for the coarsest grids. The fracture aperture at the steady state fracture length also converges as the grid is refined, Figure 12c. The S_r of the simulated fracture apertures with respect to the aperture computed through the smallest mesh size also decreases as the as the grid is refined, Figure 12d. Based on these convergence results, we adopt a mesh size $\delta x = \delta y = 1/400 = 2.5 \times 10^{-3}$.

4.4. The Effect of the Length Scale Parameter ℓ

The internal length scale ℓ plays a central role in the phase field formulation of fracture, as it behaves mathematically as a regularization parameter. We study the dependence of the fracture patterns and lengths on this intrinsic length scale by running multiple simulations with the same grid and dimensionless injection rate $q = 5 \times 10^{-5}$. We vary ℓ from 0.01 to 0.03

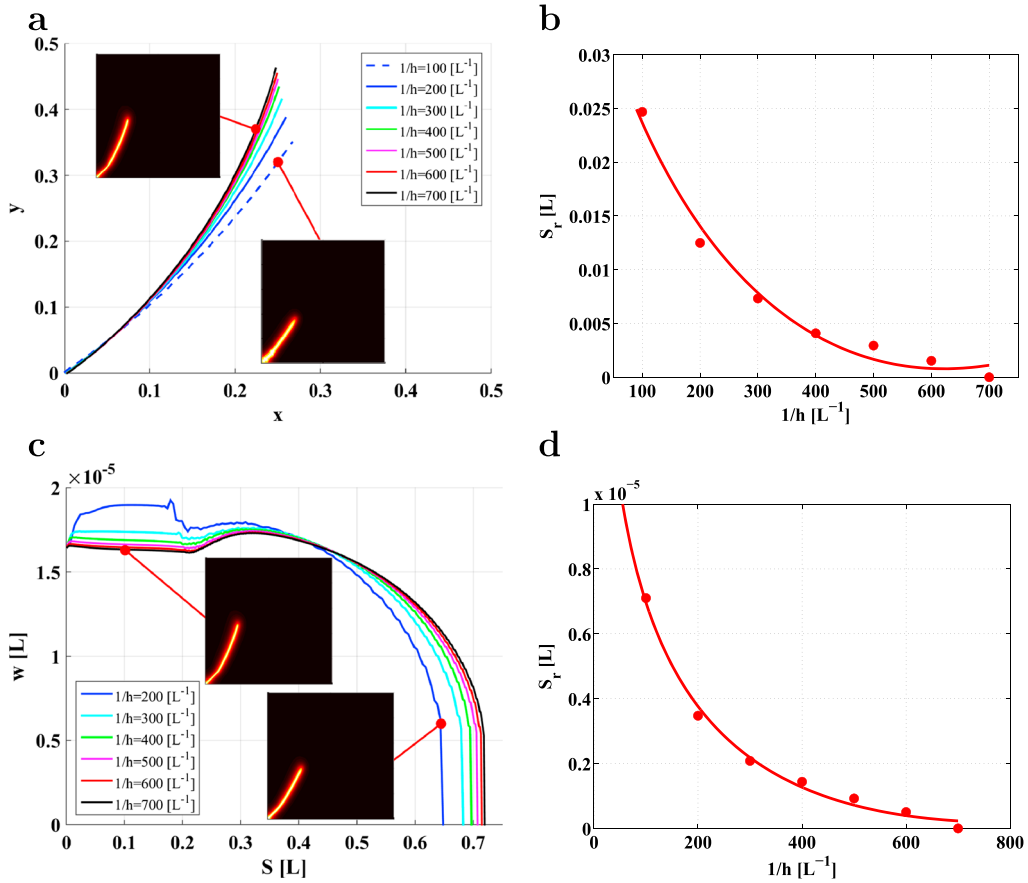

Figure 12. Mesh convergence study for arbitrary oriented fractures. The dimensionless flow rate is 5×10^{-5} and the initial strains are $\varepsilon_{yy} = 1.25 \times 10^{-5}$ and $\varepsilon_{xx} = \varepsilon_{xy} = 0$. (a) We plot the steady state fracture paths for mesh sizes ranging from 1/200 [L^{-1}] to 1/700 [L^{-1}]. (b) Here we plot the value of S_r of the fracture path for every simulation, taking as reference solution the simulation with the smallest size. The model solution converges to the reference case for increasingly fine mesh sizes. (d) We depict the steady state fracture aperture, w, for mesh sizes ranging from 1/200 [L^{-1}] to 1/700 [L^{-1}]. (d) We plot the value of S_r of the fracture aperture for every simulation, taking as reference solution the simulation with the smallest size. The model solution also converges to the reference case for increasingly fine mesh sizes.

and plot against corresponding steady state fracture lengths (Figure 13a). The fracture length varies from 0.72 for the largest value of ℓ to 0.78 for the smallest ones. The variation is only a 4% around the mean value of the fracture. A slight dependence of the fracture length on ℓ is detected: an increasing length scale results in a shorter fracture length. We also show several contour plots of the phase field variable, where it can be appreciated that the damaged zone around the fracture is wider as ℓ increases.

The pressure evolution in the injection point is plotted in Figure 13b. The evolution presents an extremely steep slope up to a time equal to approximately 20, when the fracture starts to propagate, and suddenly the pressure decreases. After that time, the pressure gradually increases up to a constant value. The length scale parameter has a minor influence on the injection pressure evolution, although a larger ℓ involves larger injection pressure.

The length scale parameter was introduced, in principle, as a mathematical parameter for approximating the Mumford-Shah potential (Mumford & Shah, 1989). However, the results of the numerical experiments reveal that it also behaves as an effective material parameter, something that has already been pointed out by several authors (Borden et al., 2012; Pham et al., 2011; Vignollet et al., 2014). Vignollet et al. (2014) reported a dependence of the peak force on the length scale parameter of a 1-D bar subjected to a constant tensile loading. The peak force decreased as the length scale parameter increased. In the present context of fluid-driven fracturing of a poroelastic medium, ℓ can be interpreted as a measure of the damaged zone around

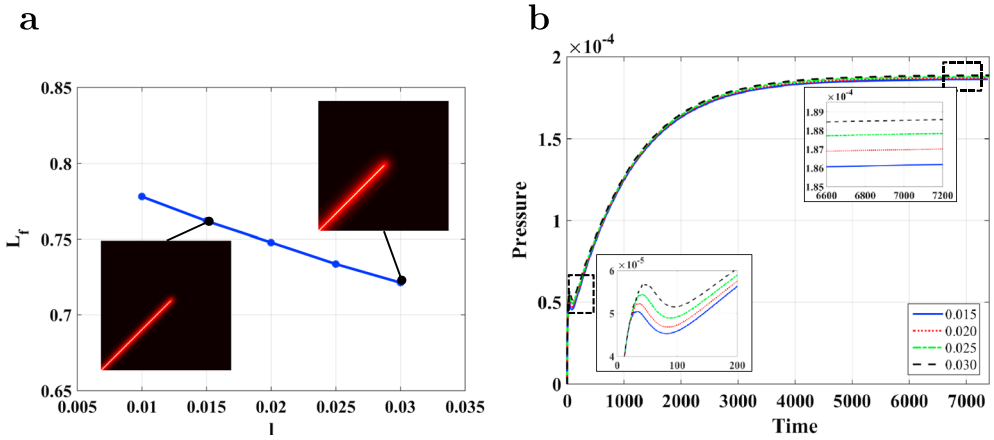

Figure 13. The internal length scale ℓ plays a central role in the phase field formulation of fracture, as it behaves as a regularization parameter. For a dimensionless injection rate of $q = 5 \times 10^{-5}$ in the quarter five-spot configuration, we show the effect of the length scale parameter ℓ on the following: (a) the steady state fracture length and (b) the injection pressure.

the fracture, that is, the phase field provides an area where the main fracture may be accompanied by a large number of much smaller fractures around it, instead of sharp fracture edges where the formation of the fracture does not imply damage in the surrounding area. This fact can be appreciated in the contour plots of Figure 13a, where the width of the damaged zone increases slightly as ℓ does.

4.5. The Effect of the Initial Fracture Length

To evaluate the effect of the initial fracture length on the steady state fracture patterns, we run a set of models whose initial dimensionless fracture length varies from 0.1 to 0.6. The dimensionless injection rate is fixed at $q = 5 \times 10^{-5}$. The initial fracture length against the final one is depicted in Figure 14a. The initial length seems to have a negligible effect on the final ones, since final lengths increase slightly as initial ones do.

The evolution of injection pressures is shown in Figure 14b for four initial lengths: 0.10, 0.15, 0.30, and 0.60. The initial length seems to have an effect on the evolution of the pressure during the initial stages: the pressure is higher as the initial fracture is shorter. Afterward, all cases have similar evolutions. Nevertheless, the stationary pressure is slightly larger as the initial fracture is shorter. This is an expected behavior because the stationary length is slightly shorter, and consequently, the injection pressure should be higher since the flow rate

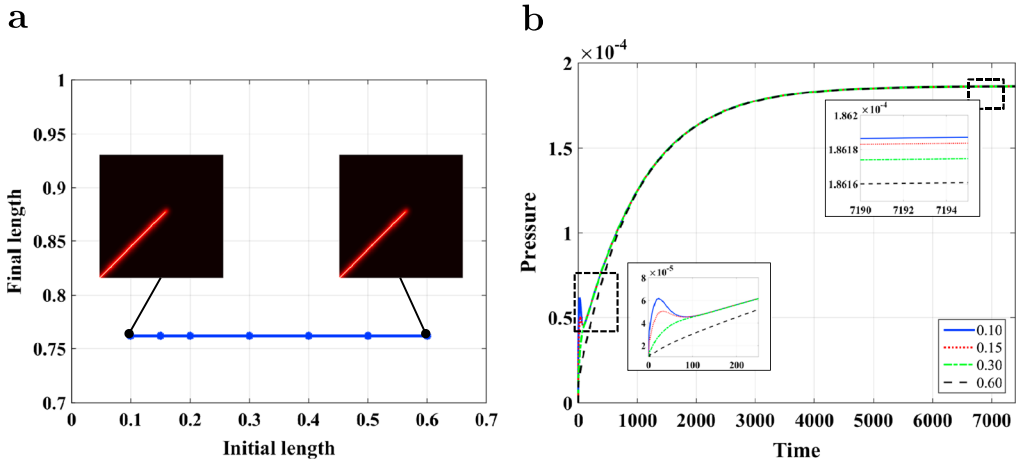

Figure 14. Effect of the initial fracture length in the quarter five-spot configuration on (a) the steady state fracture length and (b) the injection pressure. The dimensionless injection flow rate is $q = 5 \times 10^{-5}$.

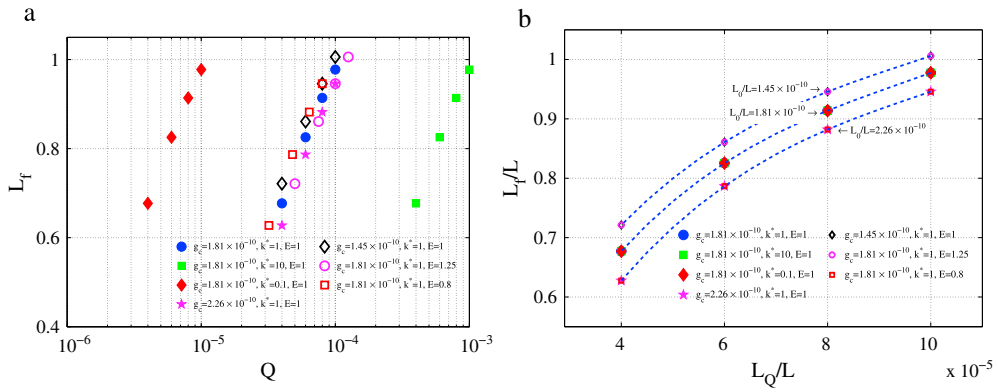

Figure 15. Stationary fracture length against injection flow rate in the quarter five-spot configuration. We run many simulations varying the permeability of the medium, the Young modulus, the Griffith critical energy release rate, and the injection flow rate. Fractures propagate in all simulations under the leak-off toughness dominated regime. (a) Stationary fracture length against flow rate in dimensional quantities for the different simulations; (a) when plotted in dimensionless quantities (see text), the data collapses along exponential-type curves whose slope decreases with L_Q/L.

is the same. In all cases, the mild dependence of pressure and phase field evolution on the initial fracture length suggests that the observed steady states are robust and physically relevant.

4.6. Parametric Study and Dimensional Analysis

We provide a dimensional analysis argument that summarizes the observed fracture behavior. We run a large set of simulations varying the medium permeability, the Young modulus, the Griffith critical energy release rate, and the injection flow rate. Fractures propagate in all simulations under the leak-off toughness dominated regime. Figure 15a summarizes the simulated results by plotting the length of the stationary fracture against the injection flow rate for different values of the aforementioned parameters. To collapse the results, we define the following four characteristics lengths: the length scale parameter, ℓ, the length of the domain, L, the Griffith length, $L_0 = g_c/E$, and the loading length, $L_Q = Q/(Ek^*)$. L_Q can be interpreted as the mechanical response or "mean fracture aperture" against Q, k^*, and E. Intuitively, the fracture aperture is directly proportional to the injection rate, since the fluid pressure increases with Q, and inversely proportional to E or k^*, as those properties measure the stiffness of the medium and the fluid leak-off from the fracture, respectively.

Taking L as reference length, we define four dimensionless numbers: L_Q/L, L_0/L, ℓ/L, and L_f/L. The parameter ℓ/L will not be considered since it is constant in all simulations and equals 0.015. The dimensionless number L_f/L is associated with the stationary fracture length. L_f/L is plotted against L_Q/L in Figure 15b for three values of L_0/L. Points collapse along an exponential-type curve whose slope increases with L_Q/L.

The effect of the hydromechanical properties on the stationary fracture length is analyzed in Figure 15b. L_f/L increases with L_Q/L, which means that the fracture is longer as the injection rate is larger or the permeability is lower. Moreover, the effect of Q can be counteracted with k^*, since while the number $L_Q/L = Q/(Ek^*)$ remains constant, L_f/L also does. This phenomenon is also presented in Figure 15a where simulations with $k^* = 0.1$, 1, 10, and, respectively, $Q = 0.1Q, Q, 10Q$ result into the same fracture length for each value of Q. The effect of g_c is analyzed through the number L_0/L. For a constant value of L_Q/L, Figures 15b shows that L_f/L increases as L_0/L decreases. Fractures propagate further in material with lower energy release rate, g_c.

The effect of the Young modulus is analyzed with both numbers L_Q/L, and L_0/L. As the modulus increases the number L_0/L decrease which, in principle, means that the fracture length becomes larger. But the number L_Q/L also decreases and the exponential shape of the curves makes this effect dominate over the previous one. As a result, the stationary fracture length is shorter as the Young modulus becomes larger.

4.7. Practical Remarks

The fluid motion in the poroelastic medium was modeled with Darcy's law solved on a regular 2-D mesh, whereas flow inside the fracture was modeled with Reynolds lubrication equation on a 1-D mesh embedded in the 2-D mesh. We suggest reducing the complexity of this approach by making two simplifications.

We propose to replace the storage term in the Reynolds lubrication equation with the storage term of the Biot poroelasticity equation. This approximation allows us to solve the problem on a unique 2-D mesh where

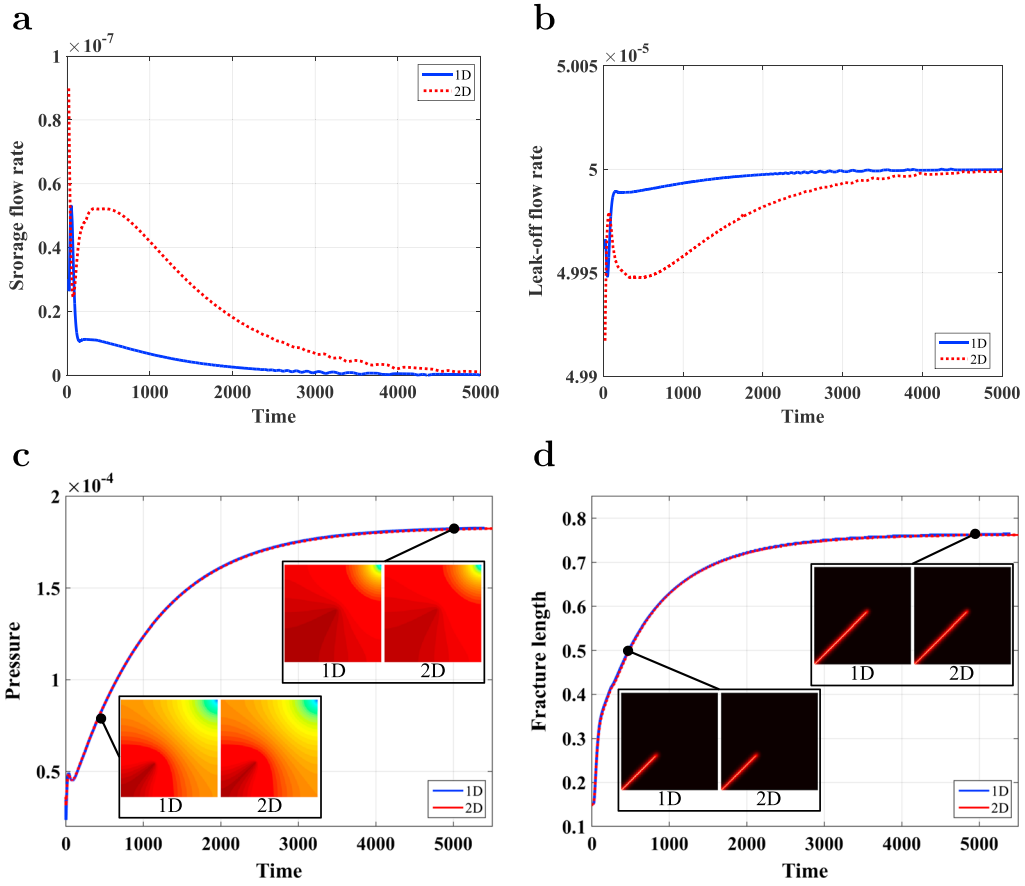

Figure 16. Decomposition of the injected fluid flow through the fracture into the following: (a) storage flow rate and (b) leak-off flow rate. The storage rate in the 2-D model is higher than in the 1-D, since it depends on the volumetric strain of the fractured nodes. Evolution of (c) injection pressure and (d) fracture length. The evolution the injection pressure and fracture length, and the pressure fields are very similar in both approaches. q is 5×10^{-5}.

the permeability of the fractured nodes is then replaced by an effective permeability in the direction of the fracture path. The effective permeability is computed through the cubic law and scaled to account for the mesh size. The permeability in the perpendicular direction accounts for leakage and can be modified if necessary.

We apply the proposed simplification to model the propagation of a fluid-driven fracture in our case study with dimensionless $q = 5 \times 10^{-5}$ and the hydromechanical properties listed in Table 1. Simulation results with the original and simplified models are given in Figure 16, where the models are denoted as 1D and 2D, respectively, in reference to the way fractures are handled.

We depict the evolution of the flow rate leaked from the fracture to the porous solid and the rate stored in the crack in Figure 16a. The storage rate in the simplified model is higher than in the original, since it depends on the volumetric strain of the fractured nodes. Phase field models regularize damage and the transition between broken and unbroken regions is spread out over a small finite region. As a result, the fractured nodes are surrounded by others with some degree of damage which induces slightly higher strains than the values provided by discrete approaches. This drawback is avoided in the original model by computing the fracture aperture with equation (58), extended over a region around the fracture. We also plot the leak-off flow rate in Figure 16b. The sum of both rates, storage and leak-off, is equal to the prescribed injection rate.

We plot the evolution of the injection pressure in Figure 16c, together with contour plots of the pressure field. The evolutions and the pressure fields for both treatments of fractures are very similar. A minor difference can be seen in the contour plots at time 500. The region with the highest pressure is extended through a smaller area in the simplified model due to the higher storage flow rate. The discrepancy disappears as the fracture propagates.

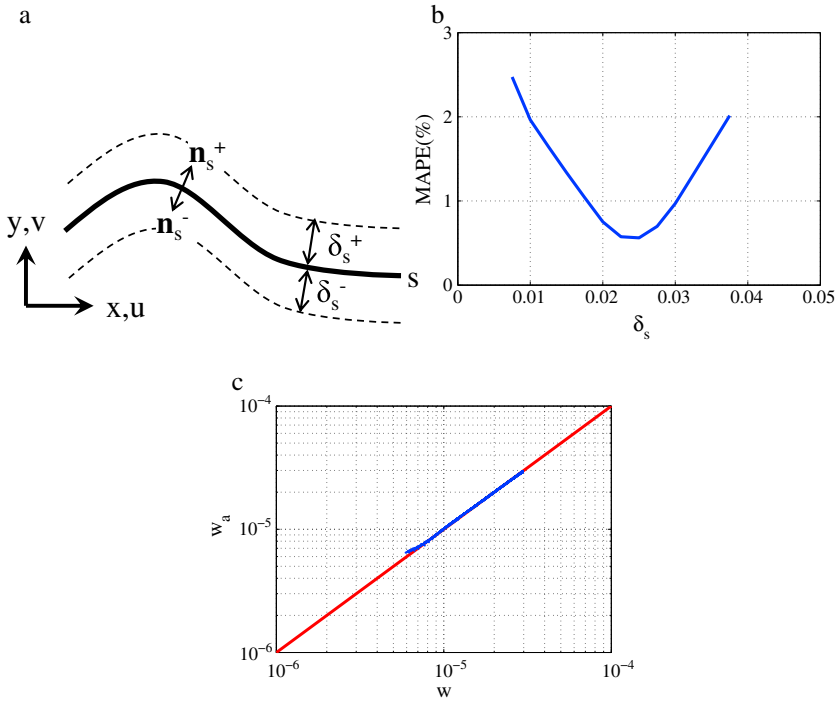

Figure 17. Evaluation of the fracture aperture using the proposed approximation, equation (96), instead of equation (58). (a) Schematic of the fracture path, unit normal vector to fracture $\mathbf{n_s}$, and parallel curves to fracture at distances δ_s. (b) Mean absolute percentage error of fracture aperture against s. (c) Plot of w against w_a for the optimal value of s for all time steps of the simulation with $q = 5 \times 10^{-5}$.

We provide the evolution of the fracture length in Figure 16d for both approaches, and some contour plots of the phase field variable. No differences are seen between both evolutions. The observed discrepancies in the storage and leak-off flow rates do not seem to significantly affect the pressure or phase field variables.

The regularization of damage involves computing the fracture aperture through equation (58). We propose an approximate but straightforward function to calculate w:

$$w(\mathbf{x},\mathbf{u},d) \approx w_a(\mathbf{x},\mathbf{u}) = \left\langle \mathbf{u}(\mathbf{x}+\delta_s), \mathbf{n}_s^+(\mathbf{x}) \right\rangle - \left\langle \mathbf{u}(\mathbf{x}), \mathbf{n}_s^+(\mathbf{x}) \right\rangle + \left\langle \mathbf{u}(\mathbf{x}-\delta_s), \mathbf{n}_s^-(\mathbf{x}) \right\rangle - \left\langle \mathbf{u}(\mathbf{x}), \mathbf{n}_s^-(\mathbf{x}) \right\rangle \quad \forall \mathbf{x} \in s \tag{96}$$

where $\langle \mathbf{a}, \mathbf{b} \rangle$ is the scalar product of vectors $\mathbf{a}$ and $\mathbf{b}$, s is the fracture path, $\mathbf{u}(\mathbf{x} \pm \delta_s)$ is the displacement of the point situated at distance $\pm\delta_s$ from $s(\mathbf{x})$, and $\mathbf{n}_s^{\pm}(\mathbf{x})$ is the unit normal to the fracture at upper and lower sides of point $\mathbf{x}$ (see Figure 17a). Points $(\mathbf{x} \pm \delta_s)$ belong to curves parallel to s at distance δ_s.

We computed *a posteriori* the fracture aperture of the simulation with $q = 5 \times 10^{-5}$ through both formulations and we calculated the mean absolute percentage error, defined by

$$\text{MAPE} = \frac{100}{N} \sum_{i=1}^{N} \left| \frac{w - w_a}{w} \right|. \tag{97}$$

We plot MAPE against δ_s in Figure 17b. The minimum error is 0.56% which corresponds to $\delta_s = 0.025$. For lower values of δ_s, w_a is higher than w due to the higher strain introduced by the regularization of the damage, and for higher values of δ_s, w_a is lower than w. We depict w_a against w for the optimal δ_s in Figure 17c in log-log scale. The computed apertures are aligned along the diagonal, which indicates that the loss of accuracy from these approximations is negligible.

5. Conclusions

Phase field models have emerged as a promising tool to simulate fluid-driven fracturing in poroelastic media. Here, we have extended a phase field model of fluid-driven fracturing in elastic media, which has been validated with analytical solutions (Santillán, Juanes, & Cueto-Felgueroso, 2017), to poroelastic media. Our model

describes the fluid flow in the fracture through the Reynolds lubrication equation, and the poroelastic medium follows the Biot poroelasticity model. A central novel aspect of our approach is the simulation of the fracture flow on a lower-dimension manifold in space with a nonlocal definition of the fracture aperture, and the use of the fluid flux between the fracture and the porous solid as coupling variable.

We have assessed our model in the quarter five-spot configuration. We have simulated the propagation of a small initial fracture located in the diagonal of the domain. The fracture started in the injection well where fluid was injected at constant rate trough the fracture. The production well was situated in the opposite corner, and fluid was extracted at constant pressure. Under this configuration, we have identified three stationary fracture patterns: (1) the fracture did not propagate, (2) the fracture propagated following a straight line and reached a robust steady state length whose magnitude depended, as expected, on the injection flow rate; and (3) the fracture propagated following a straight path up to a point where it branched into two. The transition between patterns depends on the injection flow rate. We have found that the poroelastic coupling plays a vital role on the final fracture topology: the stress induced by the pore pressure around the production well arrests the propagation of the fracture.

We have found a slight dependence of the stationary fracture length on the length scale parameter; an increasing length scale resulted in a shorter fracture length. The injection pressure evolution showed a minor dependence on this parameter; for the same flow injection rate, the pressure increases slightly as the length scale parameter increases. We have conducted a dimensional analysis, which enabled us to determine several characteristic length scales and to evaluate the physical consistency of the model. We have analyzed the effect of the hydromechanical properties and the injection flow rate on the stationary fracture length. As expected, the fracture length increases as the flow rate does, or as the hydraulic conductivity, the Griffith energy release rate or the Young modulus decrease. Finally, we have proposed two simplifications to reduce the complexity of our approach, with encouraging results under the leak-off toughness dominated fracture propagation regime.

An important problem in phase field modeling of fracture is the determination of the fracture aperture, which cannot be directly recovered from the displacement field. This is an important drawback of the phase field approach, since the aperture plays a vital role in the computation of the fluid pressure inside the fracture, which in turn controls fracture propagation and leak-off rate. Our approach incorporates a careful computation of the fracture aperture, which allows a detailed description and simulation of the fracture flow. A consequence of this description is the need for inferring the fracture path, which could be a limitation for the simulation of complex fracture topologies. Our approach captures the key controlling mechanisms of coupled flow, rock deformation, and brittle fracture mechanics and shows promise to simulate and understand more complex processes in fluid-driven fracturing of porous media.

Acknowledgments
This research was supported by the Spanish Ministry of Economy and Competitiveness under grant CTM2014-54312-P. L. C. F. also gratefully acknowledges funding from the Spanish Ministry of Economy and Competitiveness (grant RyC-2012-11704). The authors thank financial support from the MIT International Science and Technology Initiatives (MISTI) through an MIT-Spain Seed Funds award. D. S. thanks the Department of Civil and Environmental Engineering at MIT for the hospitality during his research stay from May to July 2017 and the "Universidad Politécnica de Madrid" through the "Programa Propio de I+D+i de la UPM. Convocatoria de ayudas al personal docente e investigador para estancias breves en el extranjero 2017" for its financial support. No data were used in producing this manuscript.

References

Ambati, M., Gerasimov, T., & De Lorenzis, L. (2015). A review on phase-field models of brittle fracture and a new fast hybrid formulation. *Computational Mechanics*, *55*(2), 383–405.

Ambrosio, L., & Tortorelli, V. (1990). Approximation of functional depending on jumps by elliptic functional via Γ-convergence. *Communications on Pure and Applied Mathematics*, *43*(8), 999–1036.

Aranson, I., Kalatsky, V., & Vinokur, V. (2000). Continuum field description of crack propagation. *Physical Review Letters*, *85*(1), 118.

Barry, S., & Mercer, G. (1999). Exact solutions for two-dimensional time-dependent flow and deformation within a poroelastic medium. *Journal of Applied Mechanics*, *66*, 536–540.

Biot, M. A. (1941). General theory of three-dimensional consolidation. *Journal of Applied Physics*, *12*(2), 155–164.

Biot, M. A. (1972). Theory of finite deformations of porous solids. *Indiana University Mathematics Journal*, *21*(7), 597–620.

Borden, M. J., Verhoosel, C. V., Scott, M. A., Hughes, T. J., & Landis, C. M. (2012). A phase-field description of dynamic brittle fracture. *Computer Methods in Applied Mechanics and Engineering*, *217*, 77–95.

Bouchard, P.-O., Bay, F., & Chastel, Y. (2003). Numerical modelling of crack propagation: Automatic remeshing and comparison of different criteria. *Computer Methods in Applied Mechanics and Engineering*, *192*(35), 3887–3908.

Bourdin, B., Chukwudozie, C., & Yoshioka, K. (2012). A variational approach to the numerical simulation of hydraulic fracturing. In *SPE Annual Technical Conference and Exhibition*. SPE-159154-MS. Society of Petroleum Engineers.

Bourdin, B., Francfort, G., & Marigo, J. (2000). Numerical experiments in revisited brittle fracture. *Journal of the Mechanics and Physics of Solids*, *48*(4), 797–826.

Cai, Z., & Ofterdinger, U. (2014). Numerical assessment of potential impacts of hydraulically fractured bowland shale on overlying aquifers. *Water Resources Research*, *50*, 6236–6259. https://doi.org/10.1002/2013WR014943

Carrier, B., & Granet, S. (2012). Numerical modeling of hydraulic fracture problem in permeable medium using cohesive zone model. *Engineering Fracture Mechanics*, *79*, 312–328.

Christie, M., & Blunt, M. (2001). Tenth SPE comparative solution project: A comparison of upscaling techniques. *SPE Reservoir Evaluation & Engineering*, *4*, 308–317.

Coats, K. (1982). Simulation of 1/8 five-/nine-spot patterns. *SPE Journal*, *22*(6), 902.

Cueto-Felgueroso, L., & Juanes, R. (2013). Forecasting long-term gas production from shale. *Proceedings of the National Academy of Sciences of the United States of America*, *110*(49), 19,660–19,661.
Demirdžić, I., & Martinović, D. (1993). Finite volume method for thermo-elasto-plastic stress analysis. *Computer Methods in Applied Mechanics and Engineering*, *109*(3–4), 331–349.
Detournay, E. (2016). Mechanics of hydraulic fractures. *Annual Review of Fluid Mechanics*, *48*, 311–339.
Eastgate, L., Sethna, J., Rauscher, M., Cretegny, T., Chen, C., & Myers, C. (2002). Fracture in mode I using a conserved phase-field model. *Physical Review E*, *65*(3), 036117.
Economides, M., & Nolte, K. (2000). *Reservoir stimulation*. Chichester, England: Wiley.
Francfort, G., & Marigo, J. (1998). Revisiting brittle fracture as an energy minimization problem. *Journal of the Mechanics and Physics of Solids*, *46*(8), 1319–1342.
Fu, P., Johnson, S. M., & Carrigan, C. R. (2013). An explicitly coupled hydro-geomechanical model for simulating hydraulic fracturing in arbitrary discrete fracture networks. *International Journal for Numerical and Analytical Methods in Geomechanics*, *37*(14), 2278–2300.
Griffith, A. (1921). The phenomena of rupture and flow in solids. *Philosophical Transactions of the Royal Society of London. Series A*, *221*, 163–198.
Hafver, A., Jettestuen, E., Feder, J., Meakin, P., & Malthe-Sørenssen, A. (2014). A node-splitting discrete element model for fluid–structure interaction. *Physica A: Statistical Mechanics and its Applications*, *416*, 61–79.
Haghighat, E., & Pietruszczak, S. (2016). On modeling of fractured media using an enhanced embedded discontinuity approach. *Extreme Mechanics Letters*, *6*, 10–22.
Heider, Y., & Markert, B. (2017). A phase-field modeling approach of hydraulic fracture in saturated porous media. *Mechanics Research Communications*, *80*, 38–46.
Henry, H., & Levine, H. (2004). Dynamic instabilities of fracture under biaxial strain using a phase field model. *Physical Review Letters*, *93*(10), 105504.
Hofacker, M., & Miehe, C. (2012). Continuum phase field modeling of dynamic fracture: Variational principles and staggered FE implementation. *International Journal of Fracture*, *178*(1), 113–129.
Hofacker, M., & Miehe, C. (2013). A phase field model of dynamic fracture: Robust field updates for the analysis of complex crack patterns. *International Journal for Numerical Methods in Engineering*, *93*(3), 276–301.
Hubbert, M. K., & Willis, D. G. (1972). Mechanics of hydraulic fracturing. *AIME Petroleum Transactions*, *210*, 153–168.
Karma, A., Kessler, D. A., & Levine, H. (2001). Phase-field model of mode III dynamic fracture. *Physical Review Letters*, *87*(4), 045501.
Karma, A., & Lobkovsky, A. (2004). Unsteady crack motion and branching in a phase-field model of brittle fracture. *Physical Review Letters*, *92*(24), 245510.
Lajeunesse, E., Martin, J., Rakotomalala, N., Salin, D., & Yortsos, Y. (1999). Miscible displacement in a Hele-Shaw cell at high rates. *Journal of Fluid Mechanics*, *398*, 299–319.
Lee, S., Mikelić, A., Wheeler, M. F., & Wick, T. (2016). Phase-field modeling of proppant-filled fractures in a poroelastic medium. *Computer Methods in Applied Mechanics and Engineering*, *312*, 509–541.
Lee, S., Wheeler, M. F., & Wick, T. (2016). Pressure and fluid-driven fracture propagation in porous media using an adaptive finite element phase field model. *Computer Methods in Applied Mechanics and Engineering*, *305*, 111–132.
Lee, S., Wheeler, M. F., & Wick, T. (2017). Iterative coupling of flow, geomechanics and adaptive phase-field fracture including level-set crack width approaches. *Journal of Computational and Applied Mathematics*, *314*, 40–60.
Legarth, B., Huenges, E., & Zimmermann, G. (2005). Hydraulic fracturing in a sedimentary geothermal reservoir: Results and implications. *International Journal of Rock Mechanics and Mining Sciences*, *42*(7), 1028–1041.
Lie, K. A., & Juanes, R. (2005). A front-tracking method for the simulation of three-phase flow in porous media. *Computational Geosciences*, *9*(1), 29–59.
Mauthe, S., & Miehe, C. (2017). Hydraulic fracture in poro-hydro-elastic media. *Mechanics Research Communications*, *80*, 69–83.
Miehe, C. (1998). Comparison of two algorithms for the computation of fourth-order isotropic tensor functions. *Computers & Structures*, *66*(1), 37–43.
Miehe, C., Hofacker, M., Schaenzel, L.-M., & Aldakheel, F. (2015). Phase field modeling of fracture in multi-physics problems. Part II. Coupled brittle-to-ductile failure criteria and crack propagation in thermo-elastic–plastic solids. *Computer Methods in Applied Mechanics and Engineering*, *294*, 486–522.
Miehe, C., Hofacker, M., & Welschinger, F. (2010). A phase field model for rate-independent crack propagation: Robust algorithmic implementation based on operator splits. *Computer Methods in Applied Mechanics and Engineering*, *199*(45), 2765–2778.
Miehe, C., & Mauthe, S. (2016). Phase field modeling of fracture in multi-physics problems. Part III. Crack driving forces in hydro-poro-elasticity and hydraulic fracturing of fluid-saturated porous media. *Computer Methods in Applied Mechanics and Engineering*, *304*, 619–655.
Miehe, C., Mauthe, S., & Teichtmeister, S. (2015). Minimization principles for the coupled problem of Darcy–Biot-type fluid transport in porous media linked to phase field modeling of fracture. *Journal of the Mechanics and Physics of Solids*, *82*, 186–217.
Miehe, C., Schänzel, L.-M., & Ulmer, H. (2015). Phase field modeling of fracture in multi-physics problems. Part I. Balance of crack surface and failure criteria for brittle crack propagation in thermo-elastic solids. *Computer Methods in Applied Mechanics and Engineering*, *294*, 449–485.
Miehe, C., Welschinger, F., & Hofacker, M. (2010). Thermodynamically consistent phase-field models of fracture: Variational principles and multi-field FE implementations. *International Journal for Numerical Methods in Engineering*, *83*(10), 1273–1311.
Mikelić, A., Wheeler, M., & Wick, T. (2015a). A phase-field method for propagating fluid-filled fractures coupled to a surrounding porous medium. *Multiscale Modeling & Simulation*, *13*(1), 367–398.
Mikelić, A., Wheeler, M., & Wick, T. (2015b). A quasi-static phase-field approach to pressurized fractures. *Nonlinearity*, *28*(5), 1371.
Moës, N., Dolbow, J., & Belytschko, T. (1999). A finite element method for crack growth without remeshing. *International Journal for Numerical Methods in Engineering*, *46*(1), 131–150.
Moore, T. A. (2012). Coalbed methane: A review. *International Journal of Coal Geology*, *101*, 36–81.
Mumford, D., & Shah, J. (1989). Optimal approximations by piecewise smooth functions and associated variational problems. *Communications on Pure and Applied Mathematics*, *42*(5), 577–685.
Nordbotten, J. M. (2014). Finite volume hydromechanical simulation in porous media. *Water Resources Research*, *50*, 4379–4394. https://doi.org/10.1002/2013WR015179
Osborn, S., Vengosh, A., Warner, N., & Jackson, R. (2011). Methane contamination of drinking water accompanying gas-well drilling and hydraulic fracturing. *Proceedings of the National Academy of Sciences of the United States of America*, *108*(20), 8172–8176.

Ouchi, H., Katiyar, A., York, J., Foster, J. T., & Sharma, M. M. (2015). A fully coupled porous flow and geomechanics model for fluid driven cracks: A peridynamics approach. *Computational Mechanics*, *55*(3), 561–576.

Patzek, T., Male, F., & Marder, M. (2013). Gas production in the Barnett Shale obeys a simple scaling theory. *Proceedings of the National Academy of Sciences of the United States of America*, *110*(49), 19,731–19,736.

Pham, K., Amor, H., Marigo, J.-J., & Maurini, C. (2011). Gradient damage models and their use to approximate brittle fracture.*International Journal of Damage Mechanics*, *20*(4), 618–652.

Reagan, M. T., Moridis, G. J., Keen, N. D., & Johnson, J. N. (2015). Numerical simulation of the environmental impact of hydraulic fracturing of tight/shale gas reservoirs on near-surface groundwater: Background, base cases, shallow reservoirs, short-term gas, and water transport. *Water Resources Research*, *51*, 2543–2573. https://doi.org/10.1002/2014WR016086

Réthoré, J., Borst, R., & Abellan, M. A. (2007). A two-scale approach for fluid flow in fractured porous media. *International Journal for Numerical Methods in Engineering*, *71*(7), 780–800.

Riaz, A., & Meiburg, E. (2003). Three-dimensional miscible displacement simulations in homogeneous porous media with gravity override. *Journal of Fluid Mechanics*, *494*, 95–117.

Russell, T. F., & Wheeler, M. F. (1983). Finite element and finite difference methods for continuous flows in porous media. In *The Mathematics of Reservoir Simulation* (pp. 35–106). Philadelphia: SIAM.

Santillán, D., Juanes, R., & Cueto-Felgueroso, L. (2017). Phase field model of fluid-driven fracture in elastic media: Immersed-fracture formulation and validation with analytical solutions. *Journal of Geophysical Research: Solid Earth*, *122*, 2565–2589. https://doi.org/10.1002/2016JB013572

Santillán, D., Mosquera, J. C., & Cueto-Felgueroso, L. (2017a). Phase-field model for brittle fracture. Validation with experimental results and extension to dam engineering problems. *Engineering Fracture Mechanics*, *178*, 109–125.

Santillán, D., Mosquera, J. C., & Cueto-Felgueroso, L. (2017b). Fluid-driven fracture propagation in heterogeneous media: Probability distributions of fracture trajectories. *Physical Review E*, *96*(5), 053002.

Shojaei, A., Taleghani, A. D., & Li, G. (2014). A continuum damage failure model for hydraulic fracturing of porous rocks. *International Journal of Plasticity*, *59*, 199–212.

Sneddon, I. (1946). The distribution of stress in the neighbourhood of a crack in an elastic solid. *Proceedings of the Royal Society of London A: Mathematical, Physical and Engineering Sciences*, *187*(1009), 229–260.

Spatschek, R., Brener, E., & Karma, A. (2011). Phase field modeling of crack propagation. *Philosophical Magazine*, *91*(1), 75–95.

Vidic, R., Brantley, S., Vandenbossche, J., Yoxtheimer, D., & Abad, J. (2013). Impact of shale gas development on regional water quality. *Science*, *340*(6134), 1235009.

Vignollet, J., May, S., Borst, R. D., & Verhoosel, C. (2014). Phase-field models for brittle and cohesive fracture. *Meccanica*, *49*(11), 2587–2601.

Wangen, M. (2011). Finite element modeling of hydraulic fracturing on a reservoir scale in 2D. *Journal of Petroleum Science and Engineering*, *77*(3), 274–285.

Wilson, Z. A., & Landis, C. M. (2016). Phase-field modeling of hydraulic fracture. *Journal of the Mechanics and Physics of Solids*, *96*, 264–290.

Zhang, H., Sorbie, K., & Tsibuklis, N. (1997). Viscous fingering in five-spot experimental porous media: New experimental results and numerical simulation. *Chemical Engineering Science*, *52*(1), 37–54.